Science Advances
AAAS

Supplementary Materials for

Uncovering a tripartite landmark in posterior cingulate cortex

Ethan H. Willbrand *et al.*

Corresponding author: Kevin S. Weiner, kweiner@berkeley.edu

Sci. Adv. **8**, eabn9516 (2022)
DOI: 10.1126/sciadv.abn9516

This PDF file includes:

Supplementary Text

Alzheimer's Disease Neuroimaging Initiative: group members

Michael Weiner, MD (UC San Francisco, Principal Investigator, Executive Committee); Paul Aisen, MD (UC San Diego, ADCS PI and Director of Coordinating Center Clinical Core, Executive Committee, Clinical Core Leaders); Ronald Petersen, MD, PhD (Mayo Clinic, Rochester, Executive Committee, Clinical Core Leader); Clifford R. Jack, Jr., MD (Mayo Clinic, Rochester, Executive Committee, MRI Core Leader); William Jagust, MD (UC Berkeley, Executive Committee; PET Core Leader); John Q. Trojanowki, MD, PhD (U Pennsylvania, Executive Committee, Biomarkers Core Leader); Arthur W. Toga, PhD (USC, Executive Committee, Informatics Core Leader); Laurel Beckett, PhD (UC Davis, Executive Committee, Biostatistics Core Leader); Robert C. Green, MD, MPH (Brigham and Women's Hospital, Harvard Medical School, Executive Committee and Chair of Data and Publication Committee); Andrew J. Saykin, PsyD (Indiana University, Executive Committee, Genetics Core Leader); John Morris, MD (Washington University St. Louis, Executive Committee, Neuropathology Core Leader); Leslie M. Shaw (University of Pennsylvania, Executive Committee, Biomarkers Core Leader); Enchi Liu, PhD (Janssen Alzheimer Immunotherapy, ADNI 2 Private Partner Scientific Board Chair); Tom Montine, MD, PhD (University of Washington) ; Ronald G. Thomas, PhD (UC San Diego); Michael Donohue, PhD (UC San Diego); Sarah Walter, MSc (UC San Diego); Devon Gessert (UC San Diego); Tamie Sather, MS (UC San Diego,); Gus Jiminez, MBS (UC San Diego); Danielle Harvey, PhD (UC Davis;); Michael Donohue, PhD (UC San Diego); Matthew Bernstein, PhD (Mayo Clinic, Rochester); Nick Fox, MD (University of London); Paul Thompson, PhD (USC School of Medicine); Norbert Schuff, PhD (UCSF MRI); Charles DeCArli, MD (UC Davis); Bret Borowski, RT (Mayo Clinic); Jeff Gunter, PhD (Mayo Clinic); Matt Senjem, MS (Mayo Clinic); Prashanthi Vemuri, PhD (Mayo Clinic); David Jones, MD (Mayo Clinic); Kejal Kantarci (Mayo Clinic); Chad Ward (Mayo Clinic); Robert A. Koeppe, PhD (University of Michigan, PET Core Leader); Norm Foster, MD (University of Utah); Eric M. Reiman, MD (Banner Alzheimer's Institute); Kewei Chen, PhD (Banner Alzheimer's Institute); Chet Mathis, MD (University of Pittsburgh); Susan Landau, PhD (UC Berkeley); Nigel J. Cairns, PhD, MRCPath (Washington University St. Louis); Erin Householder (Washington University St. Louis); Lisa Taylor Reinwald, BA, HTL (Washington University St. Louis); Virginia Lee, PhD, MBA (UPenn School of Medicine); Magdalena Korecka, PhD (UPenn School of Medicine); Michal Figurski, PhD (UPenn School of Medicine); Karen Crawford (USC); Scott Neu, PhD (USC); Tatiana M. Foroud, PhD (Indiana University); Steven Potkin, MD UC (UC Irvine); Li Shen, PhD (Indiana University); Faber Kelley, MS, CCRC (Indiana University); Sungeun Kim, PhD (Indiana University); Kwangsik Nho, PhD (Indiana University); Zaven Kachaturian, PhD (Khachaturian, Radebaugh & Associates, Inc and Alzheimer's Association's Ronald and Nancy Reagan's Research Institute); Richard Frank, MD, PhD (General Electric); Peter J. Snyder, PhD (Brown University); Susan Molchan, PhD (National Institute on Aging/ National Institutes of Health); Jeffrey Kaye, MD (Oregon Health and Science University); Joseph Quinn, MD (Oregon Health and Science University); Betty Lind, BS (Oregon Health and Science University); Raina Carter, BA (Oregon Health and Science University); Sara Dolen, BS (Oregon Health and Science University); Lon S. Schneider, MD (University of Southern California); Sonia Pawluczyk, MD (University of Southern California); Mauricio Beccera, BS (University of Southern California); Liberty Teodoro, RN

(University of Southern California); Bryan M. Spann, DO, PhD (University of Southern California); James Brewer, MD, PhD (University of California San Diego); Helen Vanderswag, RN (University of California San Diego); Adam Fleisher, MD (University of California San Diego); Judith L. Heidebrink, MD, MS (University of Michigan); Joanne L. Lord, LPN, BA, CCRC (University of Michigan); Ronald Petersen, MD, PhD (Mayo Clinic, Rochester); Sara S. Mason, RN (Mayo Clinic, Rochester); Colleen S. Albers, RN (Mayo Clinic, Rochester); David Knopman, MD (Mayo Clinic, Rochester); Kris Johnson, RN (Mayo Clinic, Rochester); Rachelle S. Doody, MD, PhD (Baylor College of Medicine); Javier Villanueva Meyer, MD (Baylor College of Medicine); Munir Chowdhury, MBBS, MS (Baylor College of Medicine); Susan Rountree, MD (Baylor College of Medicine); Mimi Dang, MD (Baylor College of Medicine); Yaakov Stern, PhD (Columbia University Medical Center); Lawrence S. Honig, MD, PhD (Columbia University Medical Center); Karen L. Bell, MD (Columbia University Medical Center); Beau Ances, MD (Washington University, St. Louis); John C. Morris, MD (Washington University, St. Louis); Maria Carroll, RN, MSN (Washington University, St. Louis); Sue Leon, RN, MSN (Washington University, St. Louis); Erin Householder, MS, CCRP (Washington University, St. Louis); Mark A. Mintun, MD (Washington University, St. Louis); Stacy Schneider, APRN, BC, GNP (Washington University, St. Louis); Angela Oliver, RN, BSN, MSG ; Daniel Marson, JD, PhD (University of Alabama Birmingham); Randall Griffith, PhD, ABPP (University of Alabama Birmingham); David Clark, MD (University of Alabama Birmingham); David Geldmacher, MD (University of Alabama Birmingham); John Brockington, MD (University of Alabama Birmingham); Erik Roberson, MD (University of Alabama Birmingham); Hillel Grossman, MD (Mount Sinai School of Medicine); Effie Mitsis, PhD (Mount Sinai School of Medicine); Leyla deToledo-Morrell, PhD (Rush University Medical Center); Raj C. Shah, MD (Rush University Medical Center); Ranjan Duara, MD (Wien Center); Daniel Varon, MD (Wien Center); Maria T. Greig, HP (Wien Center); Peggy Roberts, CNA (Wien Center); Marilyn Albert, PhD (Johns Hopkins University); Chiadi Onyike, MD (Johns Hopkins University); Daniel D'Agostino II, BS (Johns Hopkins University); Stephanie Kielb, BS (Johns Hopkins University); James E. Galvin, MD, MPH (New York University); Dana M. Pogorelec (New York University); Brittany Cerbone (New York University); Christina A. Michel (New York University); Henry Rusinek, PhD (New York University); Mony J de Leon, EdD (New York University); Lidia Glodzik, MD, PhD (New York University); Susan De Santi, PhD (New York University); P. Murali Doraiswamy, MD (Duke University Medical Center); Jeffrey R. Petrella, MD (Duke University Medical Center); Terence Z. Wong, MD (Duke University Medical Center); Steven E. Arnold, MD (University of Pennsylvania); Jason H. Karlawish, MD (University of Pennsylvania); David Wolk, MD (University of Pennsylvania); Charles D. Smith, MD (University of Kentucky); Greg Jicha, MD (University of Kentucky); Peter Hardy, PhD (University of Kentucky); Partha Sinha, PhD (University of Kentucky); Elizabeth Oates, MD (University of Kentucky); Gary Conrad, MD (University of Kentucky); Oscar L. Lopez, MD (University of Pittsburgh); MaryAnn Oakley, MA (University of Pittsburgh); Donna M. Simpson, CRNP, MPH (University of Pittsburgh); Anton P. Porsteinsson, MD (University of Rochester Medical Center); Bonnie S. Goldstein, MS, NP (University of Rochester Medical Center); Kim Martin, RN (University of Rochester Medical Center); Kelly M. Makino, BS (University of Rochester Medical Center); M. Saleem Ismail, MD (University of Rochester Medical Center); Connie Brand, RN (University of Rochester Medical Center); Ruth A. Mulnard, DNSc, RN, FAAN (University of California, Irvine); Gaby Thai, MD (University of

California, Irvine); Catherine Mc Adams Ortiz, MSN, RN, A/GNP (University of California, Irvine); Kyle Womack, MD (University of Texas Southwestern Medical School); Dana Mathews, MD, PhD (University of Texas Southwestern Medical School); Mary Quiceno, MD (University of Texas Southwestern Medical School); Ramon Diaz Arrastia, MD, PhD (University of Texas Southwestern Medical School); Richard King, MD (University of Texas Southwestern Medical School); Myron Weiner, MD (University of Texas Southwestern Medical School); Kristen Martin Cook, MA (University of Texas Southwestern Medical School); Michael DeVous, PhD (University of Texas Southwestern Medical School); Allan I. Levey, MD, PhD (Emory University); James J. Lah, MD, PhD (Emory University); Janet S. Cellar, DNP, PMHCNS BC (Emory University); Jeffrey M. Burns, MD (University of Kansas, Medical Center); Heather S. Anderson, MD (University of Kansas, Medical Center); Russell H. Swerdlow, MD (University of Kansas, Medical Center); Liana Apostolova, MD (University of California, Los Angeles); Kathleen Tingus, PhD (University of California, Los Angeles); Ellen Woo, PhD (University of California, Los Angeles); Daniel H.S. Silverman, MD, PhD (University of California, Los Angeles); Po H. Lu, PsyD (University of California, Los Angeles); George Bartzokis, MD (University of California, Los Angeles); Neill R Graff Radford, MBBCH, FRCP (London) (Mayo Clinic, Jacksonville); Francine Parfitt, MSH, CCRC (Mayo Clinic, Jacksonville); Tracy Kendall, BA, CCRP (Mayo Clinic, Jacksonville); Heather Johnson, MLS, CCRP (Mayo Clinic, Jacksonville); Martin R. Farlow, MD (Indiana University); Ann Marie Hake, MD (Indiana University); Brandy R. Matthews, MD (Indiana University); Scott Herring, RN, CCRC (Indiana University); Cynthia Hunt, BS, CCRP (Indiana University); Christopher H. van Dyck, MD (Yale University School of Medicine); Richard E. Carson, PhD (Yale University School of Medicine); Martha G. MacAvoy, PhD (Yale University School of Medicine); Howard Chertkow, MD (McGill Univ., Montreal Jewish General Hospital); Howard Bergman, MD (McGill Univ., Montreal Jewish General Hospital); Chris Hosein, Med (McGill Univ., Montreal Jewish General Hospital); Sandra Black, MD, FRCPC (Sunnybrook Health Sciences, Ontario); Dr Bojana Stefanovic (Sunnybrook Health Sciences, Ontario); Curtis Caldwell, PhD (Sunnybrook Health Sciences, Ontario); Ging Yuek Robin Hsiung, MD, MHSc, FRCPC (U.B.C. Clinic for AD & Related Disorders); Howard Feldman, MD, FRCPC (U.B.C. Clinic for AD & Related Disorders); Benita Mudge, BS (U.B.C. Clinic for AD & Related Disorders); Michele Assaly, MA Past (U.B.C. Clinic for AD & Related Disorders); Andrew Kertesz, MD (Cognitive Neurology St. Joseph's, Ontario); John Rogers, MD (Cognitive Neurology St. Joseph's, Ontario); Dick Trost, PhD (Cognitive Neurology St. Joseph's, Ontario); Charles Bernick, MD (Cleveland Clinic Lou Ruvo Center for Brain Health); Donna Munic, PhD (Cleveland Clinic Lou Ruvo Center for Brain Health); Diana Kerwin, MD (Northwestern University); Marek Marsel Mesulam, MD (Northwestern University); Kristine Lipowski, BA (Northwestern University); Chuang Kuo Wu, MD, PhD (Northwestern University); Nancy Johnson, PhD (Northwestern University); Carl Sadowsky, MD (Premiere Research Inst (Palm Beach Neurology)); Walter Martinez, MD (Premiere Research Inst (Palm Beach Neurology)); Teresa Villena, MD (Premiere Research Inst (Palm Beach Neurology)); Raymond Scott Turner, MD, PhD (Georgetown University Medical Center); Kathleen Johnson, NP (Georgetown University Medical Center); Brigid Reynolds, NP (Georgetown University Medical Center); Reisa A. Sperling, MD (Brigham and Women's Hospital); Keith A. Johnson, MD (Brigham and Women's Hospital); Gad Marshall, MD (Brigham and Women's Hospital); Meghan Frey (Brigham and Women's Hospital); Jerome Yesavage, MD (Stanford University); Joy L.

Taylor, PhD (Stanford University); Barton Lane, MD (Stanford University); Allyson Rosen, PhD (Stanford University); Jared Tinklenberg, MD (Stanford University); Marwan N. Sabbagh, MD (Banner Sun Health Research Institute); Christine M. Belden, PsyD (Banner Sun Health Research Institute); Sandra A. Jacobson, MD (Banner Sun Health Research Institute); Sherye A. Sirrel, MS (Banner Sun Health Research Institute); Neil Kowall, MD (Boston University); Ronald Killiany, PhD (Boston University); Andrew E. Budson, MD (Boston University); Alexander Norbash, MD (Boston University); Patricia Lynn Johnson, BA (Boston University); Thomas O. Obisesan, MD, MPH (Howard University); Saba Wolday, MSc (Howard University); Joanne Allard, PhD (Howard University); Alan Lerner, MD (Case Western Reserve University); Paula Ogrocki, PhD (Case Western Reserve University); Leon Hudson, MPH (Case Western Reserve University); Evan Fletcher, PhD (University of California, Davis Sacramento); Owen Carmichael, PhD (University of California, Davis Sacramento); John Olichney, MD (University of California, Davis Sacramento); Charles DeCarli, MD (University of California, Davis Sacramento); Smita Kittur, MD (Neurological Care of CNY); Michael Borrie, MB ChB (Parkwood Hospital); T Y Lee, PhD (Parkwood Hospital); Dr Rob Bartha, PhD (Parkwood Hospital); Sterling Johnson, PhD (University of Wisconsin); Sanjay Asthana, MD (University of Wisconsin); Cynthia M. Carlsson, MD (University of Wisconsin); Steven G. Potkin, MD (University of California, Irvine BIC); Adrian Preda, MD (University of California, Irvine BIC); Dana Nguyen, PhD (University of California, Irvine BIC); Pierre Tariot, MD (Banner Alzheimer's Institute); Adam Fleisher, MD (Banner Alzheimer's Institute); Stephanie Reeder, BA (Banner Alzheimer's Institute); Vernice Bates, MD (Dent Neurologic Institute); Horacio Capote, MD (Dent Neurologic Institute); Michelle Rainka, PharmD, CCRP (Dent Neurologic Institute); Douglas W. Scharre, MD (Ohio State University); Maria Kataki, MD, PhD (Ohio State University); Anahita Adeli, MD (Ohio State University); Earl A. Zimmerman, MD (Albany Medical College); Dzintra Celmins, MD (Albany Medical College); Alice D. Brown, FNP (Albany Medical College); Godfrey D. Pearlson, MD (Hartford Hosp, Olin Neuropsychiatry Research Center); Karen Blank, MD (Hartford Hosp, Olin Neuropsychiatry Research Center); Karen Anderson, RN (Hartford Hosp, Olin Neuropsychiatry Research Center); Robert B. Santulli, MD (Dartmouth Hitchcock Medical Center); Tamar J. Kitzmiller (Dartmouth Hitchcock Medical Center); Eben S. Schwartz, PhD (Dartmouth Hitchcock Medical Center); Kaycee M. Sink, MD, MAS (Wake Forest University Health Sciences); Jeff D. Williamson, MD, MHS (Wake Forest University Health Sciences); Pradeep Garg, PhD (Wake Forest University Health Sciences); Franklin Watkins, MD (Wake Forest University Health Sciences); Brian R. Ott, MD (Rhode Island Hospital); Henry Querfurth, MD (Rhode Island Hospital); Geoffrey Tremont, PhD (Rhode Island Hospital); Stephen Salloway, MD, MS (Butler Hospital); Paul Malloy, PhD (Butler Hospital); Stephen Correia, PhD (Butler Hospital); Howard J. Rosen, MD (UC San Francisco); Bruce L. Miller, MD (UC San Francisco); Jacobo Mintzer, MD, MBA (Medical University South Carolina); Kenneth Spicer, MD, PhD (Medical University South Carolina); David Bachman, MD (Medical University South Carolina); Elizabether Finger, MD (St. Joseph's Health Care); Stephen Pasternak, MD (St. Joseph's Health Care); Irina Rachinsky, MD (St. Joseph's Health Care); John Rogers, MD (St. Joseph's Health Care); Andrew Kertesz, MD (St. Joseph's Health Care); Dick Drost, MD (St. Joseph's Health Care); Nunzio Pomara, MD (Nathan Kline Institute); Raymundo Hernando, MD (Nathan Kline Institute); Antero Sarrael, MD (Nathan Kline Institute); Susan K. Schultz, MD (University of Iowa College of Medicine, Iowa City); Laura L. Boles Ponto,

PhD (University of Iowa College of Medicine, Iowa City); Hyungsub Shim, MD (University of Iowa College of Medicine, Iowa City); Karen Elizabeth Smith, RN (University of Iowa College of Medicine, Iowa City); Norman Relkin, MD, PhD (Cornell University); Gloria Chaing, MD (Cornell University); Lisa Raudin, PhD (Cornell University); Amanda Smith, MD (University of South Florida: USF Health Byrd Alzheimer's Institute); Kristin Fargher, MD (University of South Florida: USF Health Byrd Alzheimer's Institute); Balebail Ashok Raj, MD (University of South Florida: USF Health Byrd Alzheimer's Institute)

Supplementary Results

Algorithmically determined sulcal depth vs. post-mortem values

To relate algorithmically determined depth (Methods) (*75*) of posteromedial (PMC) sulci *in- vivo* compared to previously published manual depths of PMC sulci in post-mortem samples, we compared the ranges of algorithmically determined sulcal depth values (in mm) in the present study to post-mortem depth values (in mm) collected by Ono *et al.* (*46*). In their work, Ono and colleagues (*46*) analyzed the sulcal anatomy of 25 autopsy specimens (sex and age information was not available). Of interest to the present study, the authors computed the depth ranges of three PMC sulci analyzed in the present work: the marginal ramus of the cingulate sulcus (*mcgs*), splenial sulcus (*spls*), and parieto-occipital suclus (*pos*) (*46*). By comparing the range of the sulcal depths of the *mcgs, spls,* and *pos* (in a subset of 25 participants in each sample), we found that the algorithmically determined depth values coincided with the range of values obtained by Ono *et al.* (*46*) in the left (*mcgs* = 2-17, *spls* = 3-13, *pos* = 12-33) and right hemisphere (*mcgs* = 4-21, *spls* = 2-18, *pos* = 17-40) in both the discovery (left: *mcgs* = 12.1-18.4, *spls* = 7.6-14.9, *pos* = 15.4-23.6; right: *mcgs* = 11.7-17.3, *spls* = 6.4-14, *pos* = 17.4-25.8) and replication (left: *mcgs* = 12-18.6, *spls* = 9.7-16.1, *pos* = 11.9-23.6; right: *mcgs* = 6.9-17.6, *spls* = 6.3-13.9, *pos* = 15.2-24.3) samples. This supports the accuracy of the depth estimations obtained by the algorithm on PMC sulci.

PMC sulci are morphologically distinct

To statistically compare the raw depths (in mm) of every PMC sulcus, we ran 2-way ANOVAs with sulcus (*11 PMC sulci*) and hemisphere (*left, right*) as factors for both the discovery and replication samples.

Discovery sample: We observed a main effect of sulcus ($F(10, 706) = 268.58$, $p < 0.001$, $\eta^2G = 0.79$) and a trending effect of hemisphere ($F(1, 706) = 3.67$, $p = 0.056$, $\eta^2G = 0.005$), in which sulci in the left hemisphere were deeper (**Fig. S2A**). Post hoc tests on the former effect revealed three takeaways regarding the PRC sulci. First, the three *prcus* sulci were the shallowest of the PRC sulci, but deeper on average than the putative PCC tertiary sulci (p-values < 0.001, Tukey's adjustment; **Fig. S2A**). Second, the *prcus-p* was shallower than *prcus-i* and *prcus-a* (p-values < 0.001), while *prcus-i* and *prcus-a* had comparable depths ($p > 0.05$, Tukey's adjustment; **Fig. S2A**). Third, the *prculs* was shallower than the *pos* ($p < 0.001$, Tukey's adjustment; **Fig. S2A**).

Replication sample: Once again, main effects of sulcus ($F(10, 702) = 302.94$, $p < 0.001$, $\eta^2G = 0.81$) and hemisphere were observed ($F(1, 702) = 19.83$, $p < 0.001$, $\eta^2G = 0.03$). For the latter main effect, the PMC sulci were once again deeper in the left hemisphere on average (**Fig. S2B**). Post hoc tests on the former main effect confirmed the three main findings in the discovery sample (**Fig. S2B**). Lastly, there was an interaction between sulcus and hemisphere ($F(10, 702) = 2.17$, $p = 0.02$, $\eta^2G = 0.03$). Post hoc analyses indicated that the effect was driven by the *mcgs* and *prcus-a* being significantly deeper in the left hemisphere (p-values < 0.05, Tukey's adjustment; **Fig. S2B**).

Connectivity fingerprints of the *ifrms* and *spls* differ by hemisphere

In addition to the sulcus x network interaction discussed in the main text, we also observed a sulcus x network x hemisphere interaction in both samples (discovery: $F(5, 175) = 3.27$, $p = 0.007$, $\eta 2G = 0.02$; replication: $F(5, 165) = 8.51$, $p < 0.001$, $\eta 2G = 0.04$). In the discovery sample, i) the *ifrms* overlapped more with DMN-a in the left hemisphere than the right ($p = 0.002$, Tukey's adjustment; **Fig. 4B**, left), ii) the *spls* with the CCN-b in the right hemisphere than the left ($p = 0.002$, Tukey's adjustment; **Fig. 4B**, left), and iii) the *spls* with the DMN-b in the left hemisphere than the right ($p < 0.001$, Tukey's adjustment; **Fig. 4B**, right). These three findings were replicated in the replication sample (p-values < 0.001, Tukey's adjustment; **Fig. S9**); however, the *ifrms* also overlapped more with CCN-c in the right hemisphere than the left ($p < 0.001$, Tukey's adjustment; **Fig. S9**; see **Fig. S10** for the connectivity profiles of the *ifrms* and *spls* in all participants in the replication sample).

The three prcus components are functionally distinct from each other

Since this was the first time that three separate *prcus* sulcal components were defined within every hemisphere in a large sample, we tested if these sulci were also distinguishable based on their functional connectivity profiles. Thus, we ran a 3-way repeated measures ANOVA with sulcus (*prcus-p, prcus-i, prcus-a*), network (17 resting-state networks) (*42*), and hemisphere (*left*, *right*) as factors.

Discovery sample: We observed an interaction between sulcus and network ($F(32, 1120) = 27.98$, $p < 0.001$, $\eta^2G = 0.13$). Post hoc tests indicated that these three sulci differed in their overlap with the different default mode subnetworks. On the one hand, these sulci show a posterior to anterior decrease in the amount of overlap with DMN-a (*p*-values < 0.001, Tukey's adjustment; **Fig.**

S11A). On the other hand, the three *prcus* show a posterior to anterior increase in overlap with DMN-c (*p*-values < 0.01, Tukey's adjustment; **Fig. S11A**). Each sulcus also overlapped with other networks that were not shared with the other two sulci (**Fig. S11A**). *Prcus-p* also overlapped with CCN-b (*p*-values < 0.001, Tukey's adjustment). *Prcus-i* and *prcus-a* both overlapped more with dorsal attention network A than *prcus-p* (*p*-values < 0.001, Tukey's adjustment). *Prcus-a* also overlapped more with somatomotor network A (*p*-values < 0.01, Tukey's adjustment) and ventral attention network B (*p*-values < 0.001, Tukey's adjustment) than the other two *prcus* components, as well as overlapped more with ventral attention network A ($p = 0.001$, Tukey's adjustment) and visual network B ($p = 0.03$, Tukey's adjustment) than *prcus-p*. Altogether, the three *prcus* are functionally dissociable.

Replication sample: Here we also observed a sulcus x network interaction ($F(32, 1056) = 27.34$, $p < 0.001$, $\eta^2G = 0.2$). Post hoc tests revealed somewhat similar relationships to those observed in the discovery sample. Similar to the discovery sample, these sulci showed a posterior to anterior decrease in DMN-a overlap and a posterior to anterior increase in overlap with DMN-c (*p*-values < 0.001, Tukey's adjustment; **Fig. S11B**). Each sulcus also overlapped with other networks than the DMN (**Fig. S11B**). *Prcus-a* overlapped more with CCN-b than *prcus-i* ($p = 0.04$, Tukey's adjustment). Furthermore, *prcus-a* overlapped more with ventral attention network A, ventral attention network B, and visual network B than the other two sulci (*p*- values < 0.01, Tukey's adjustment). Finally, *prcus-i* and *prcus-a* overlapped more with dorsal attention network A than *prcus-p* (*p*-values < 0.05, Tukey's adjustment).

The *ifrms* as a functional landmark: Additional parcellations and meta-analyses

Documenting structure-function relationships is important for understanding how the brain organizes functional information (maps, networks, regions) in a predictable manner or not relative to the folding of the cerebral cortex. Yet it is equally as important to know the conditions in which a documented structure-function relationship no longer occurs. For example, the reader may ask: Is this structure-function relationship specific to the parcellation by Kong and colleagues (*42*) or to analyses performed in individual participants? In other words, does the structure-function relationship generalize to other parcellations and other types of analyses? To address these concerns, we implemented a two-fold approach. First, to test if the *ifrms*-functional correspondence was specific to the parcellation by Kong and colleagues (*42*), we defined the same sulci in PCC and PRC in individuals from the Midnight Scan Club (MSC; see **Fig. S12** for the 192 sulcal definitions across these participants) (*43*) and calculated connectivity fingerprints of the *ifrms* and *spls* in each MSC participant with the goal of testing if the structure-function relationship documented in the HCP participants would generalize to MSC participants and different network parcellations compared to those of Kong et al. (*42*) used in our initial analyses (**Fig. S13A**). Second, we tested if this structure-function relationship also generalized to group or meta-analyses.

This two-fold approach revealed that our results generalize to a different parcellation in individual participants. Specifically, after defining all PCC and PRC sulci in each MSC participant, we calculated the dice coefficient between the following regions that were cortically proximal to the *ifrms* and *spls*: (1) Fronto-Parietal (FP), (2) Default Mode (DM), (3) Parietal Memory (PM), (4) Contextual (C), (5) Cingulo-Opercular (CO), and (6) Salience (S). We report three main findings. First, we could identify the *ifrms* in every MSC participant (**Fig. S12**). Second, we replicate our main findings that the *spls* overlaps with a hub of the default mode network, while

the *ifrms* more frequently overlaps with regions neighboring the default mode hub—in this case, FP or PM regions. Specifically, a 3-way repeated-measures ANOVA with hemisphere (LH, RH), network (FP, DM, PM, C, CO, S), and sulcus (*ifrms*, *spls*) again revealed a sulcus x network interaction ($F(5,45)=10.23$, $p < 0.001$, $\eta^2G = 0.22$) in which the *ifrms* overlapped more with the PM and FP than did the *spls* ($p < 0.001$, Tukey's adjustment), while the *spls* overlapped consistently more with the DM than did the *ifrms* ($p < 0.001$, Tukey's adjustment; **Fig. S13B**). Third, as in our original analyses (**Figs. S8 and S10**), there are also individual differences in this structure-function correspondence in the MSC (**Figs. S13 and S14**). In some individuals, the structure-function correspondence between the *ifrms* and a small functional region neighboring a large hub of the DM is extremely strong, with a high dice coefficient; in others, the correspondence is weaker, reflecting the high individual variability in this parcellation. Most prominently, the FP node in PCC has extensive inter- and intra-participant variability in its size and presence (**Figure S13**) (*43, 82*). For example, some lack this node in both hemispheres (e.g., MSC07 and MSC08), while others have it in one (e.g., MSC01 and MSC10) or both (e.g., MSC02 and MSC09) hemispheres. When present, this node can range in size from small (e.g., MSC03 and MSC06) to large (e.g., MSC02 and MSC09). Thus, an immediate goal of future work will be to identify anatomical, functional, and potentially cognitive factors that contribute to the variability of this structure-function relationship across individuals.

This two-fold approach also revealed that our results are not specific to analyses conducted at the level of individual participants, but rather extend to both group and meta-analyses. In terms of group analyses (**Fig. S25B**), the *ifrms* identified on the FreeSurfer average surface (fsaverage) is situated within area 23d, as identified using multimodal criteria averaged across two separate splits of hundreds of participants from Glasser and colleagues (*44*). In terms of meta-analyses, we

projected maps for "cognitive control," "frontoparietal," and "default mode" from Neurosynth (*40*) to the MNI2009b surface, as these maps mirrored the labels used to describe the regions identified in our analyses in individual participants. Mirroring our individual and group analyses, the *ifrms* (see **Fig. S15A** for the position of *ifrms* on MNI2009b surface) co-localized with a small cognitive control cluster that overlapped with a frontoparietal cluster (more so with uniformity vs. association tests) that was ventral to, and much smaller than, the default mode region (**Fig. S15B**). These analyses indicate that this structure-function coupling extends to over 1,000 studies and is independent of the term used to refer to this region.

Directly related to this, a recent preprint showed that this cortical locus underneath the *mcgs* has little agreement across researchers regarding network membership (*45*). Thus, we also considered a combinatory meta-analysis across the association terms suggested by the authors (cognitive control, frontoparietal, executive, demand (proxy for multiple demand), and domain general). Once again, there was a focal cluster neighboring the DM hub that overlapped with the *ifrms*, with variable convergence across these terms depending on whether association or uniformity tests were performed (**Fig. S15C**).

Altogether, these analyses indicate that the *ifrms* co-localizes with a focal, functional region neighboring a large hub of the default mode network consistently across parcellations in individual participants, as well as group analyses averaged across hundreds of participants and meta-analyses averaged across hundreds of studies. This structural-functional coupling generalized across analysis types (individual participant analyses, as well as group and meta-analyses) and different functional parcellations of PCC. Complementing this consistency, the variability we observed may reflect individual differences in the location and morphology of the *ifrms* relative to recently identified connector “hubs” that integrate information between cognitive

control and default mode networks or between different cognitive control networks, which would be critical for integrating information between networks (*60*). Thus, this variability may further suggest that the small functional regions overlapping the *ifrms* may contain subpopulations of neurons that vary in their task-active and task-negative activity levels, which can be tested in future research.

Inframarginal cortical indentations in Old World monkeys, New World monkeys, and non- human hominoids: From dimple to tertiary sulcus

To determine if the cortical indentations below the *mcgs* were also present beyond our *in vivo* chimpanzee and human hemispheres, we leveraged Retzius' classic atlas (*81*) that contained photographs of post-mortem brains from Old and New World monkeys, as well as a variety of non-human hominoids (gorillas, orangutans, and chimpanzees). Here, we found that a shallow dimple (which we refer to as an inframarginal dimple, *ifrmd)* was also variably present in 63.83% (30/47) of Old World monkey hemispheres and 40% (4/10) of New World monkey hemispheres, which is consistent with references to a posterior cingulate dimple in modern research mentioned in **Figure S1**. The *ifrms* was also present in a majority of non-human hominoid hemispheres examined. Specifically, we could identify the *ifrms* in post-mortem chimpanzees (*Troglodytes Niger*; 83.33% (15/18 hemispheres)), gorillas (*Anthropopithecus Gorilla;* 75% (3/4 hemispheres), and orangutans (*Simia Satyrus*; 75% (6/8 hemispheres)) examined. Interestingly, when the *ifrmd* or *ifrms* was present, Retzius sometimes depicted it in the schematic without a label, while in others, he excluded it entirely. **Figure S21** contains some example hemispheres with the *ifrmd* or *ifrms* identified in these species. We also will include a collection of all inspected hemispheres on our lab website with the publication of this paper.

On the historical use of the term "inframarginal"

To our knowledge, throughout neuroanatomical history, a label of "inframarginal sulcus" has not been proposed previously. Nevertheless, from our historical analyses, "inframarginal convolution" or "gyrus inframarginalis inferior" was proposed in the 1800s. Specifically, Ecker (*83*) credited Huschke (*84*) for the inframarginal label. However, Huschke did not label the sulcus of interest in the present work. Instead, Huschke provided an alternative label (*gyrus inframarginalis*) for the Superior Temporal Gyrus (STG). In the description of the *Lobulus supra-marginalis*, Ecker writes (from the 1873 English translation) (*85*):

"This lobule lies between the lower end of the posterior central convolution and the upper end of the *fissura Sylvii*, and arises from the lower end of the former, which forms the posterior part of the operculum, then develops into a lobule, consisting of several convolutions, arched around the end of the *fissura Sylvii*, in order to become the lower boundary of this fissure as the *gyrus marginalis inferior* or *temporalis superior* (*T1*)."

In the description of the gyrus temporalis superior, Ecker directly references Huschke when he writes (*85*): "1. *Gyrus temporalis superior* (Huschke) *seu infra-marginalis*, upper temporal convolution (*T1*)."

Together, these historical analyses reveal that the term "inframarginal" has been used to label a part of the cortex, the STG, but not the sulcus of interest in the present study. Finally, the term inframarginal convolution has been largely removed from the modern nomenclature (*86, 87*) and therefore, will not be confusable with the name we propose for the present sulcus of interest

in the human brain.

Even Einstein has an *ifrms*

Historically, there has been great interest in "rare" brains – whether from those who have assassinated political figures or from "geniuses" (*88–90*). In terms of the latter, in the last few decades, several papers have been published regarding Albert Einstein's brain (*91–97*), including one which aimed to identify sulcal patterns that differed in Einstein compared to "typical" brains (**Fig. S26**) (*91*). This study highlighted the sulcal pattern within PCC as "abnormal" compared to "typical" sulcal patterns. The authors write:

"(F) Figure 8 of the left medial surface of Einstein's brain with unusual features highlighted in yellow. The cingulate gyrus has a long unnamed sulcus, and the cingulate sulcus gives off four inferiorly directed branches (two of which are tiny), which suggest that the cingulate gyrus may be relatively convoluted. The cuneus appears to be unusually convoluted."

Upon inspection of the published images, we have been able to identify one of these "tiny" sulci as the *ifrms*, and the other as the putative tertiary sulcus labeled here as the *icgs-p* (**Fig. S26**). An additional sulcus labeled "u" for unnamed sulcus, is an additional sulcus within the cingulate gyrus that was not explicitly quantified in the present study but that is rather common in individual hemispheres. We include this point because it stresses the importance of identifying all sulci—including shallow, tertiary sulci—of the cerebral cortex in order to accurately assess typicality and atypicality, as well as how individual differences in sulcal patterning relate to function, anatomy, and cognition in both typical and atypical brains. In this particular case, the omission of the *ifrms* and other "tiny" or shallow sulci in PCC in neuroanatomical atlases resulted in the inaccurate

conclusion that this was a special feature of Einstein's brain. Instead, this sulcal patterning in Einstein's PCC is actually common in humans, and also in many chimpanzee brains, as we quantify in the present paper.

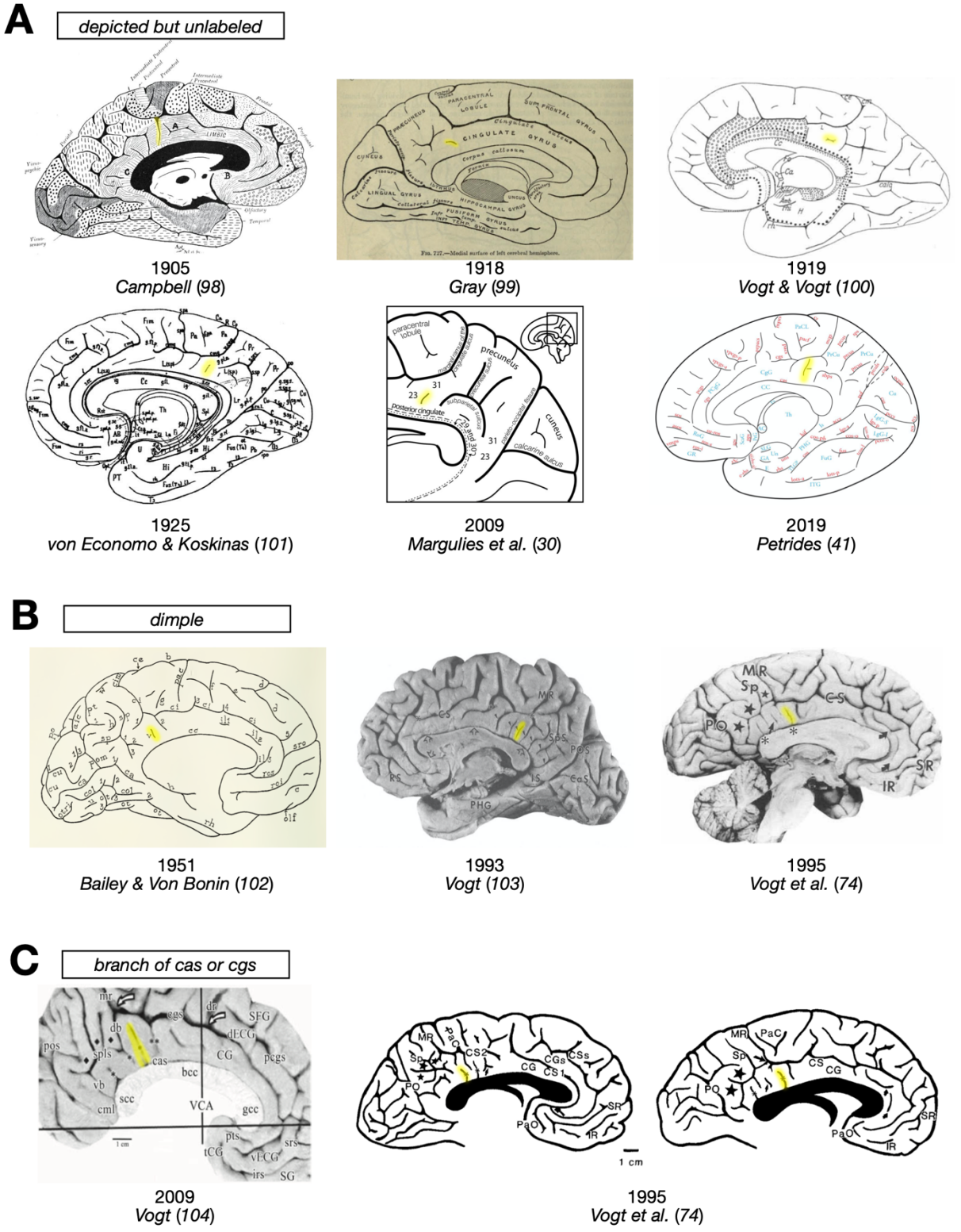

Figure S1. Shallow PCC tertiary sulci depicted, but without formal names: A synopsis of historical and modern images. It is important to note that, while this is the first time the *ifrms* and other shallow tertiary sulci were defined and labeled in a large sample, this is not the first time they have been depicted.

A. Classic and modern studies have noted the presence of a cortical indentation below the *mcgs*, but did not explicitly label it. Schematic illustrations from Campbell (*98*), Gray (*99*), Vogt and Vogt (*100*), von Economo and Koskinas (*101*), Marguiles *et al.* (*30*), and Petrides (*41*) are depicted. Yellow shading has been added to each of these images to indicate the location of the *ifrms* in the present study. **B**. In other situations, past research has also referred to the *ifrms* and the other shallow PCC tertiary sulci as inconsistent dimples. For example, Bailey and Von Bonin (*102*) referred to this indentation underneath the *mcgs* as "dimple v," while Vogt and colleagues (*74, 103*) referred to it as one of many shallow dimples in PCC (arrowhead and arrow in the middle and right images, respectively). **C**. Finally, previous work has referred to cortical indentations underneath the *mcgs* as branches of the callosal sulcus (*cas*) or cingulate sulcus (*cgs*) (*74, 104*).

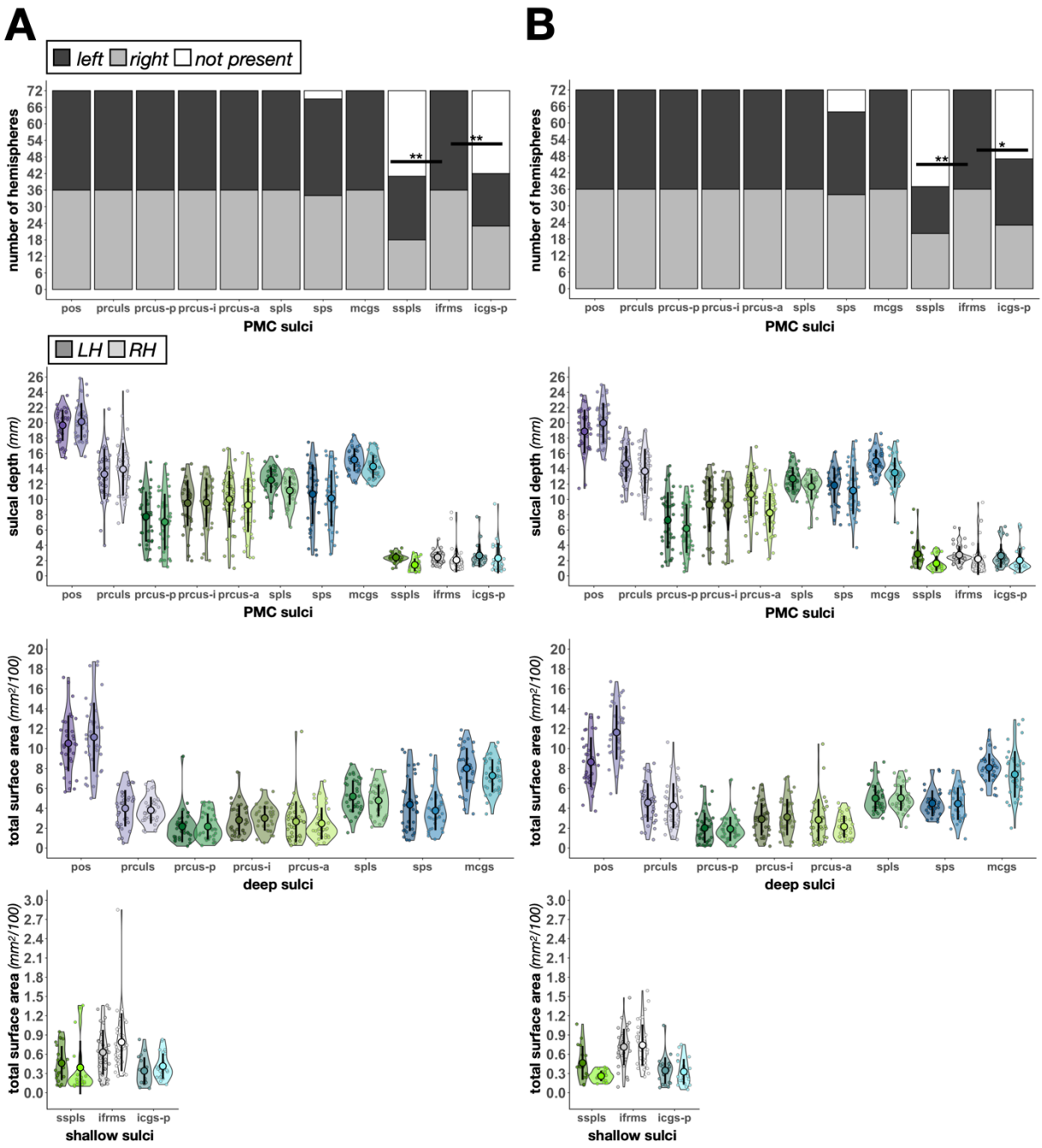

Figure S2. The *ifrms*, but not other shallow sulci in PCC, are identifiable in every hemisphere. The same layout as Figure 2, B–E, but for all 11 PMC sulci. **A.** Incidence and morphology of PMC sulci in the discovery sample. **B.** Same as A but for the replication sample. First row: Stacked bar plots illustrate the incidence rates of three shallow sulci (*ifrms, sspls, icgs-p*) relative to the other manually defined PMC sulci

(N_{total} = 72 hemispheres each). Dark gray, light gray, and white indicate the number of hemispheres that contain that given sulcus (LH: dark gray; RH: light gray; white: absent). Asterisks indicate statistically significant incidence rates between the *ifrms* and the two other shallow sulci (*p<.05, **p<0.01; the same as in Fig. 2, B and D). Second row: Sulcal depth (mm) plotted for each individual participant (small colored circles). The mean (large colored circles), standard deviation (black line), and kernel density estimate (colored violin) are also plotted for each sulcus. The PMC sulci are each colored according to the legend in Figure 2A, with darker shades indicating LH values and lighter shades indicating RH values. Third row: Same as the second row but for the total surface area (mm^2) of the deep sulci. Note that these values are scaled down by a factor of 100. Fourth row: Same as the third row, but for the three shallow sulci.

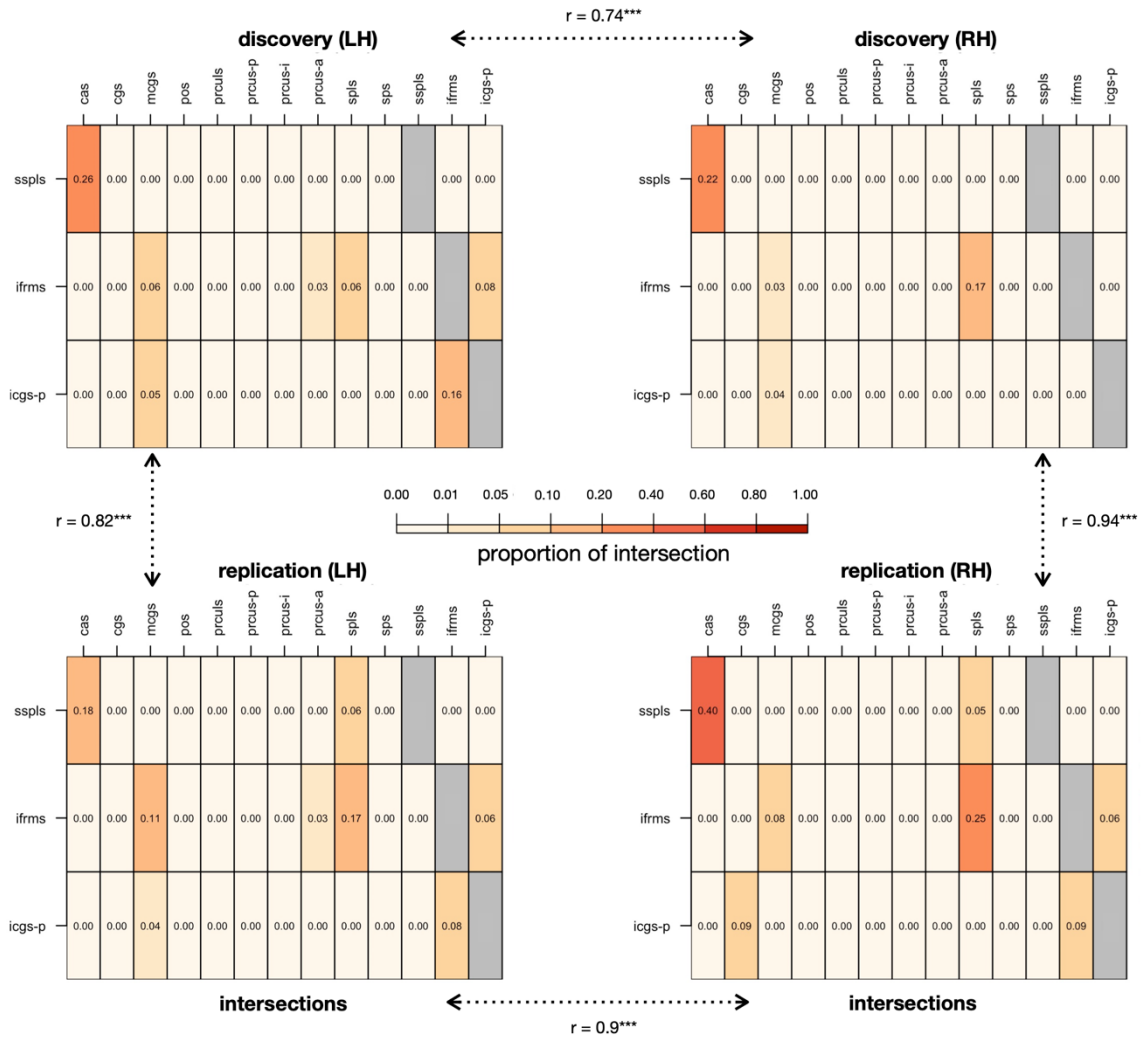

Figure S3. Intersections of shallow PCC sulci are similar between hemispheres and samples. Rates of intersection with surrounding sulci were quantified for each PCC shallow sulcus to identify common sulcal patterns in each young adult sample. For each shallow PCC sulcus (*sspls, ifrms, icgs-p*), we report the proportion of intersection (frequency of occurrence/total number of observations) with each PMC sulcus. Note that the callosal sulcus (*cas*) and cingulate sulcus (*cgs*) were also included as the *sspls* intersected with the *cas* and the *icgs-p* intersected with the *cgs* frequently. Calculating the correlation between matrices shows that intersections of these sulci is comparable (all *r*s > .70; all *p*s < 0.001) between hemispheres and samples. The three most prevalent types for each shallow sulcus in each sample are included in Tables S4 and S6.

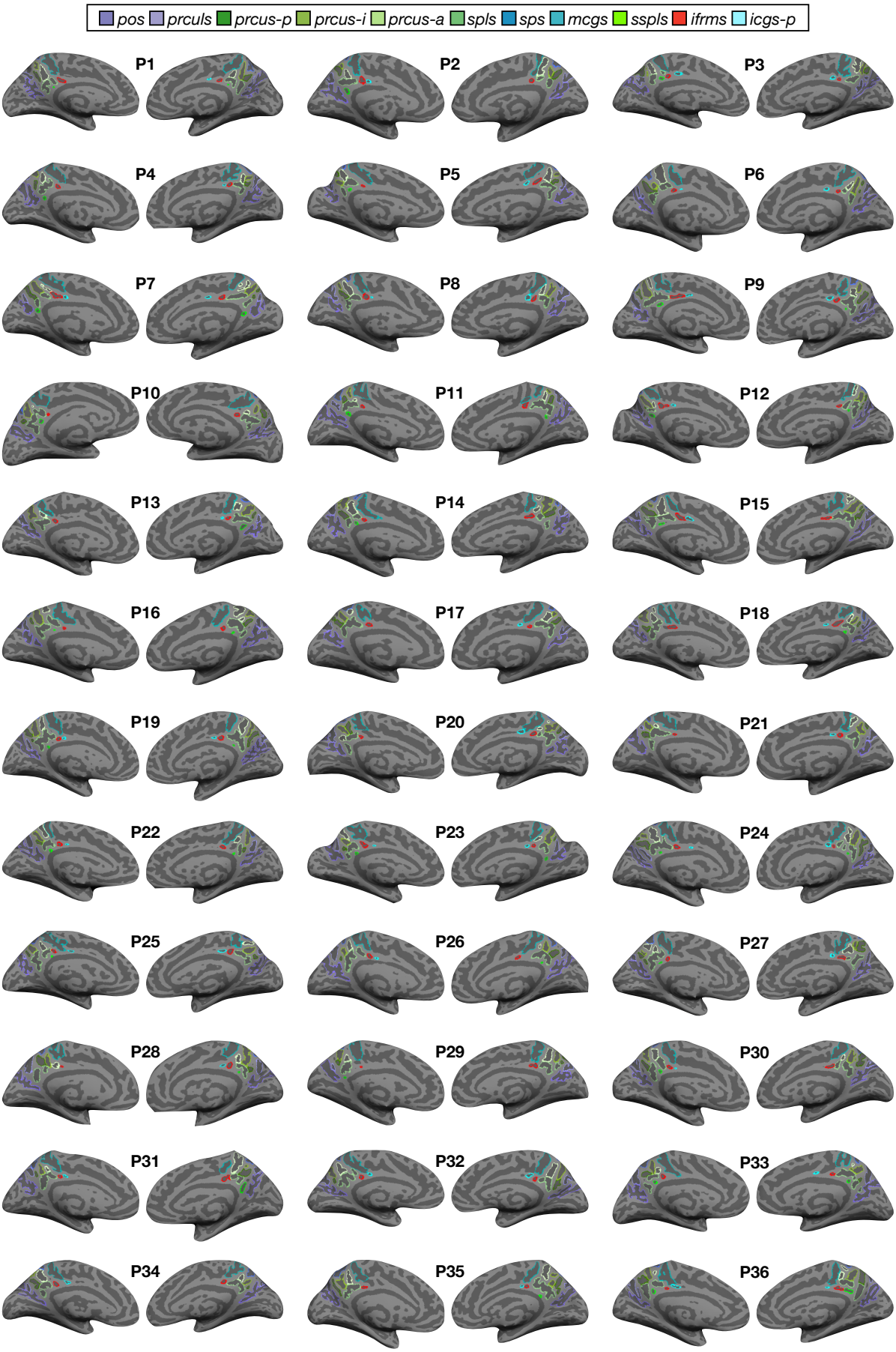
pos
prculs
prcus-p
prcus-i
prcus-a
spls
sps
mcgs
sspls
ifrms
icgs-p
P1
P2
P3
P4
P5
P6
P7
P8
P9
P10
P11
P12
P13
P14
P15
P16
P17
P18
P19
P20
P21
P22
P23
P24
P25
P26
P27
P28
P29
P30
P31
P32
P33
P34
P35
P36

Figure S4. Manual PMC sulcal labels in the left and right hemispheres of each participant in the discovery sample. Each sulcus is displayed on the inflated cortical surface in FreeSurfer 6.0.0 and is colored according to the key at the top. Each hemisphere contains at least eight sulci (from posterior to anterior): *pos, prculs, prcus-p, prcus-i, prcus-a, spls, mcgs,* and *ifrms*. The *sps*, *sspls*, and *icgs-p* are all variably present.

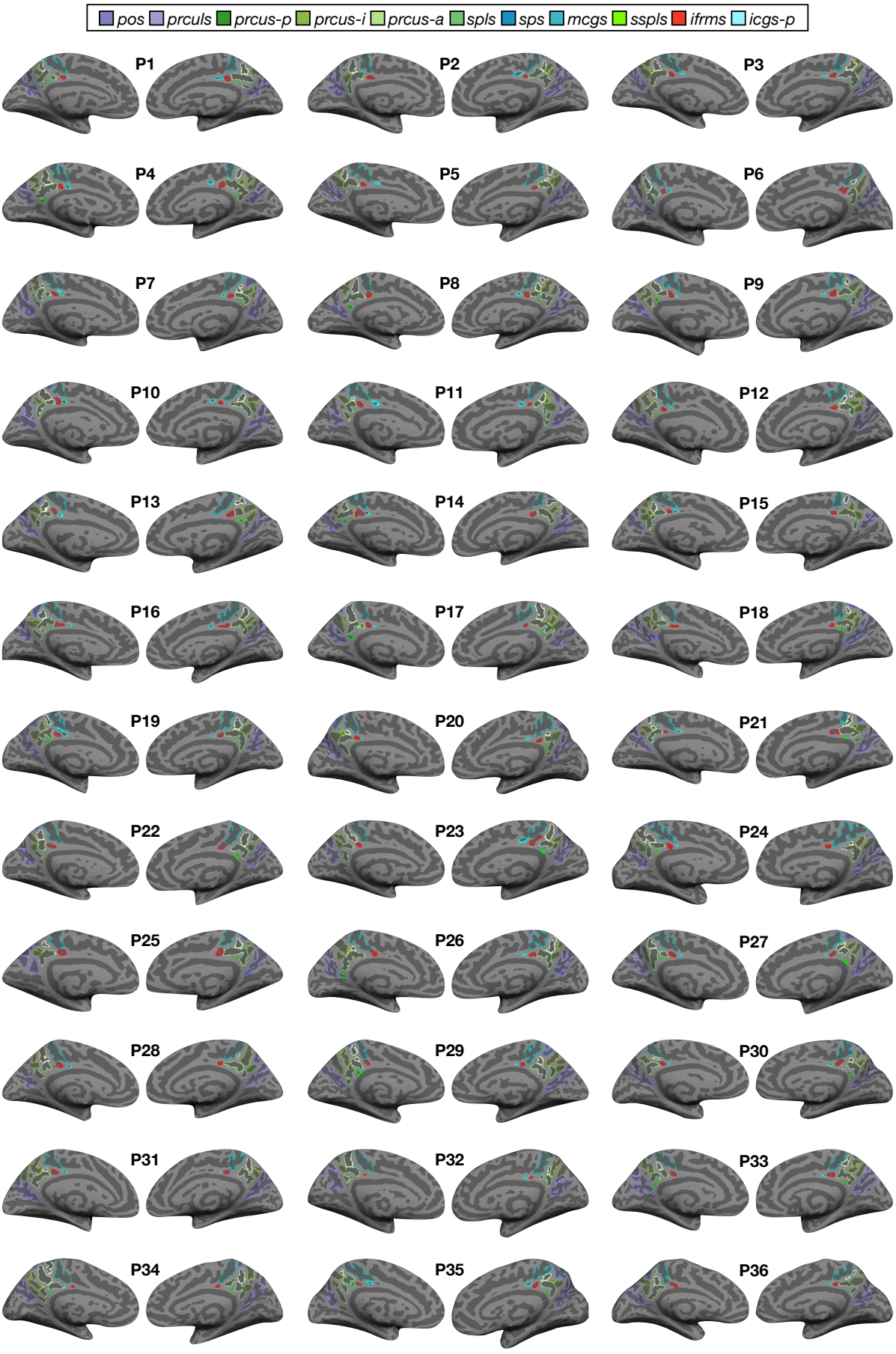
pos
prculs
prcus-p
prcus-i
prcus-a
spls
sps
mcgs
sspls
ifrms
icgs-p
P1
P2
P3
P4
P5
P6
P7
P8
P9
P10
P11
P12
P13
P14
P15
P16
P17
P18
P19
P20
P21
P22
P23
P24
P25
P26
P27
P28
P29
P30
P31
P32
P33
P34
P35
P36

Figure S5. Manual PMC sulcal labels in the left and right hemispheres of each participant in the replication sample. Same layout as Figure S4, but for the replication sample.

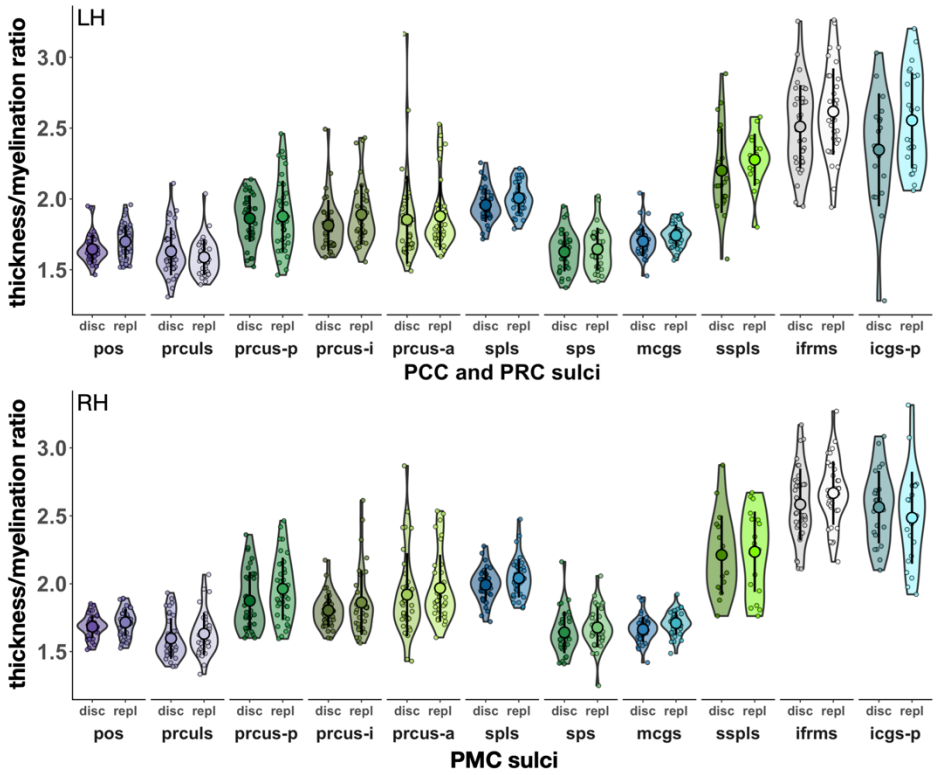

Figure S6. **The *ifrms* is a macroanatomical and microstructural landmark in PCC.** Same layout as Figure 4B. Thickness/myelination ratio for all 11 PCC sulci in the discovery (disc) and replication (repl) samples in the LH (top) and RH (bottom). Individual participants from the discovery and replication samples (small colored circles), means (large colored circles), standard deviation (black line), and kernel density estimate (colored violins) are plotted for each sulcus. For all PCC sulci, the *ifrms* has the largest thickness/myelination ratio.

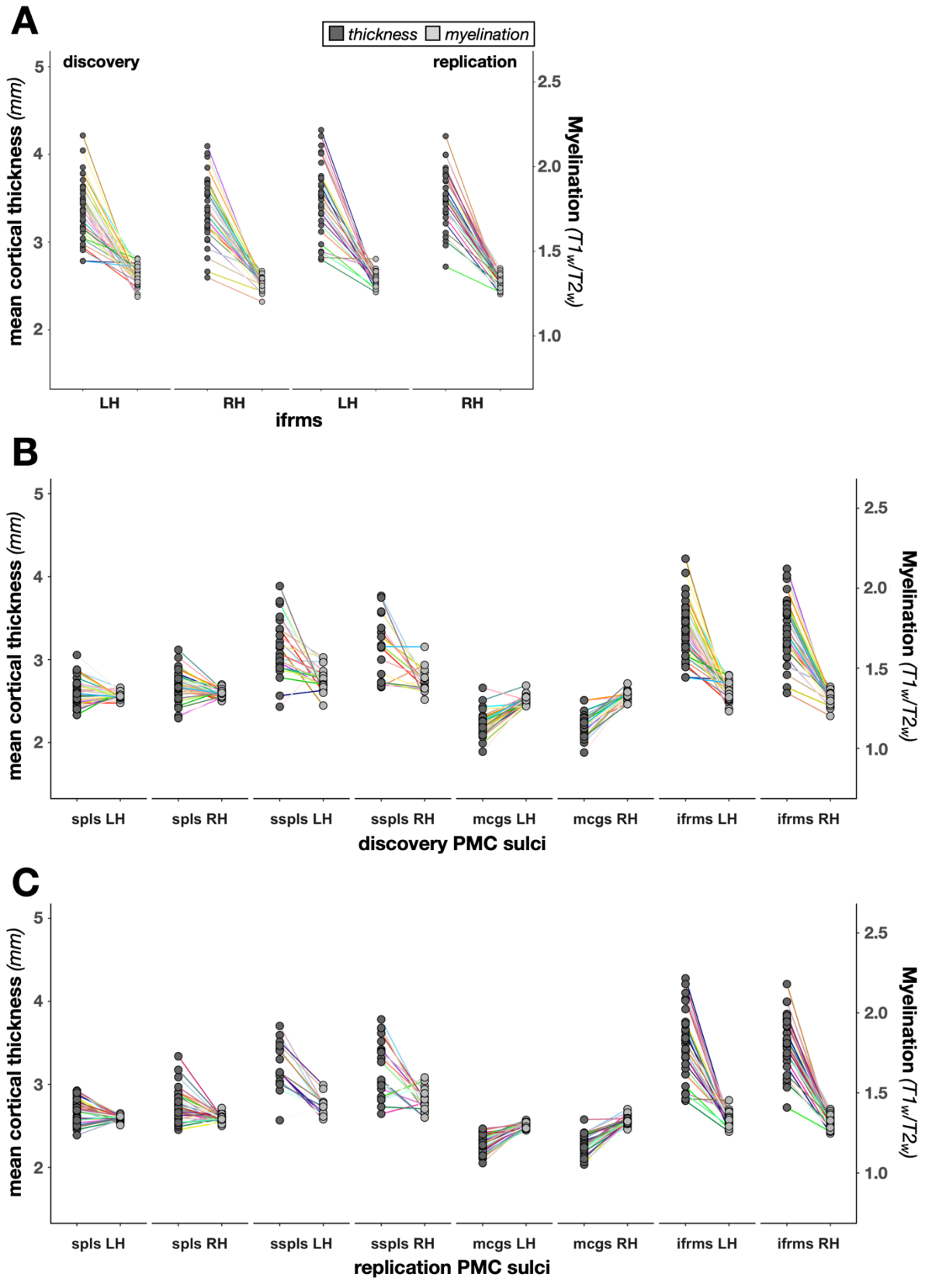

Figure S7. **Individual cortical thickness and myelination values of PMC sulci. A.** Thickness (mm; left

axis; dark gray) and myelination (T_1w/T_2w; right axis; light gray) values for the *ifrms* only in the discovery (left) and replication (right) samples in both the left (LH) and right hemispheres (RH). The thickness and myelination values for each individual participant (small circles) are plotted with a uniquely colored line connecting them. **B**. Similar layout as A, but also including the other three sulci (*spls*, *sspls*, and *mcgs*) analyzed in Figure 4B (discovery sample only). **C.** Same layout as B but for the replication sample.

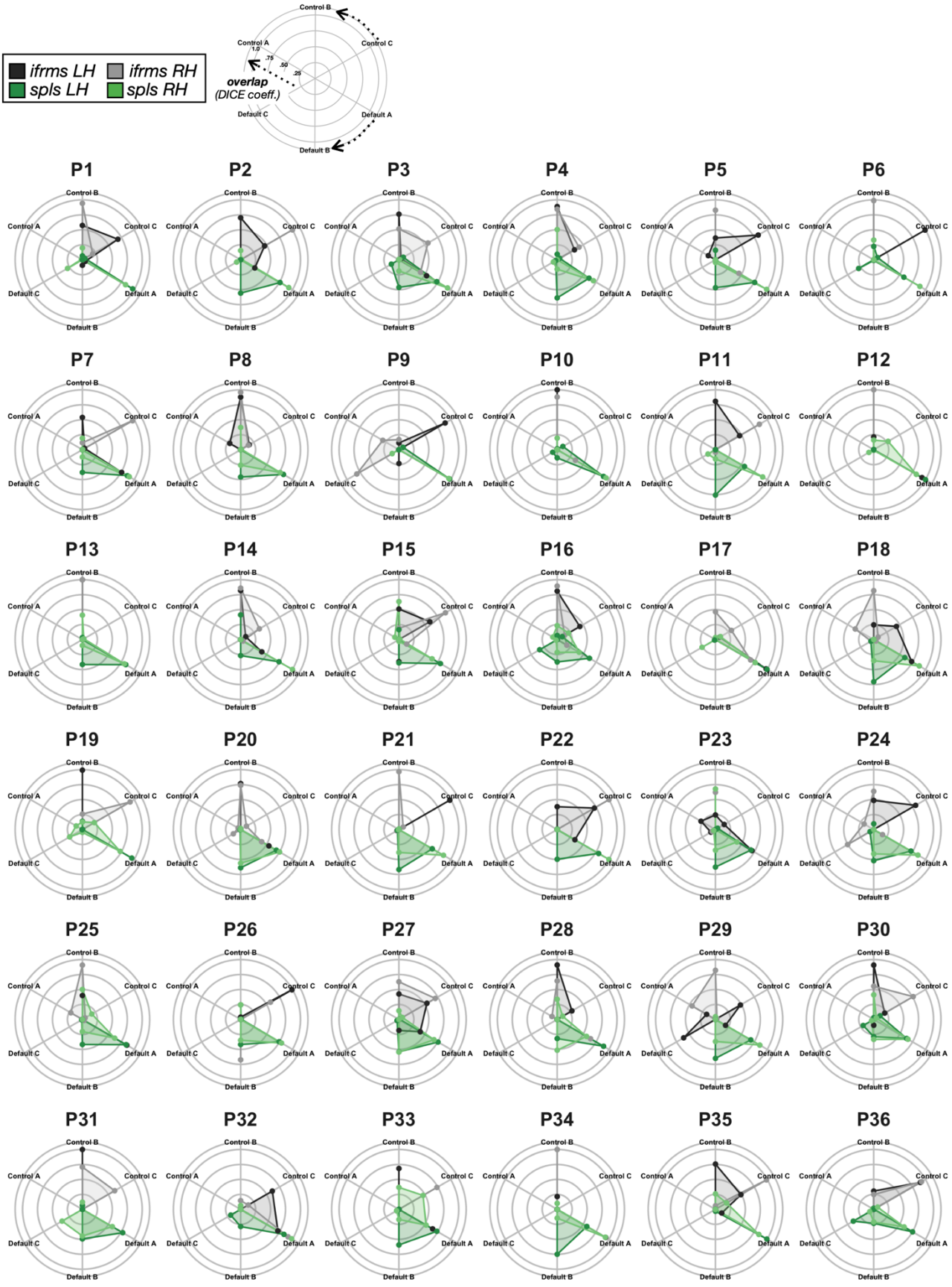
ifrms LH
ifrms RH
spls LH
spls RH
overlap
(DICE coeff.)
1.0
.75
.50
.25
Control A
Control B
Control C
Default A
Default B
Default C
P1
P2
P3
P4
P5
P6
P7
P8
P9
P10
P11
P12
P13
P14
P15
P16
P17
P18
P19
P20
P21
P22
P23
P24
P25
P26
P27
P28
P29
P30
P31
P32
P33
P34
P35
P36

Figure S8. Individual participant connectivity fingerprints of the *ifrms* and *spls* in the discovery sample. Top left: Legend for interpreting the polar plots. Arrows denote the direction of each network's overlap (CCN: top; DMN: bottom). The more the fingerprint extends to the periphery of the circle, the higher the dice coefficient. Individual participant resting state functional connectivity parcellations were obtained from a recent study (*42*), blind to cortical folding, and independent of our PMC sulcal definitions. The connectivity fingerprint represents the overlap of each network within a given sulcus. Bottom: Polar plots showing the connectivity fingerprints of the *ifrms* (grayscale) and *spls* (green) in individual participants for the left hemisphere (LH, darker shade) and right hemisphere (RH, lighter shade) of the discovery sample. Solid lines: mean. Dashed lines: ±1 SEm.

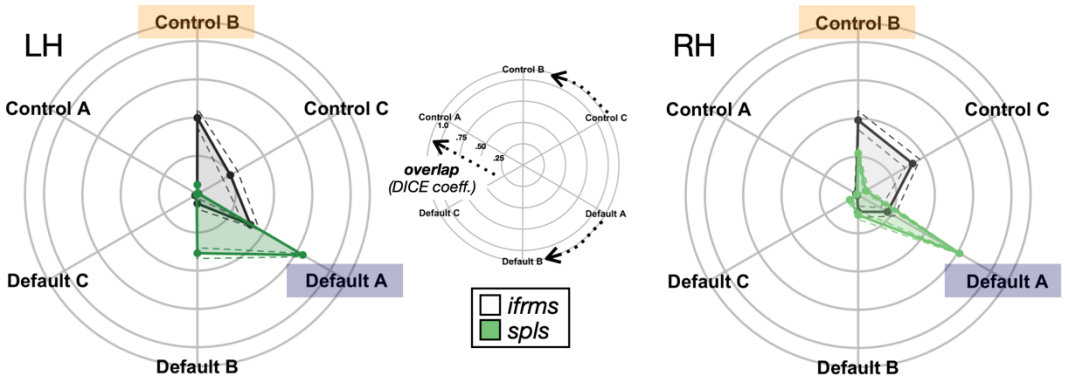

Figure S9. Mean connectivity fingerprints of the *ifrms* and *spls* in the replication sample. Same layout as Figure 5B, but for the replication sample. See Figure S10 for all individuals in this sample.

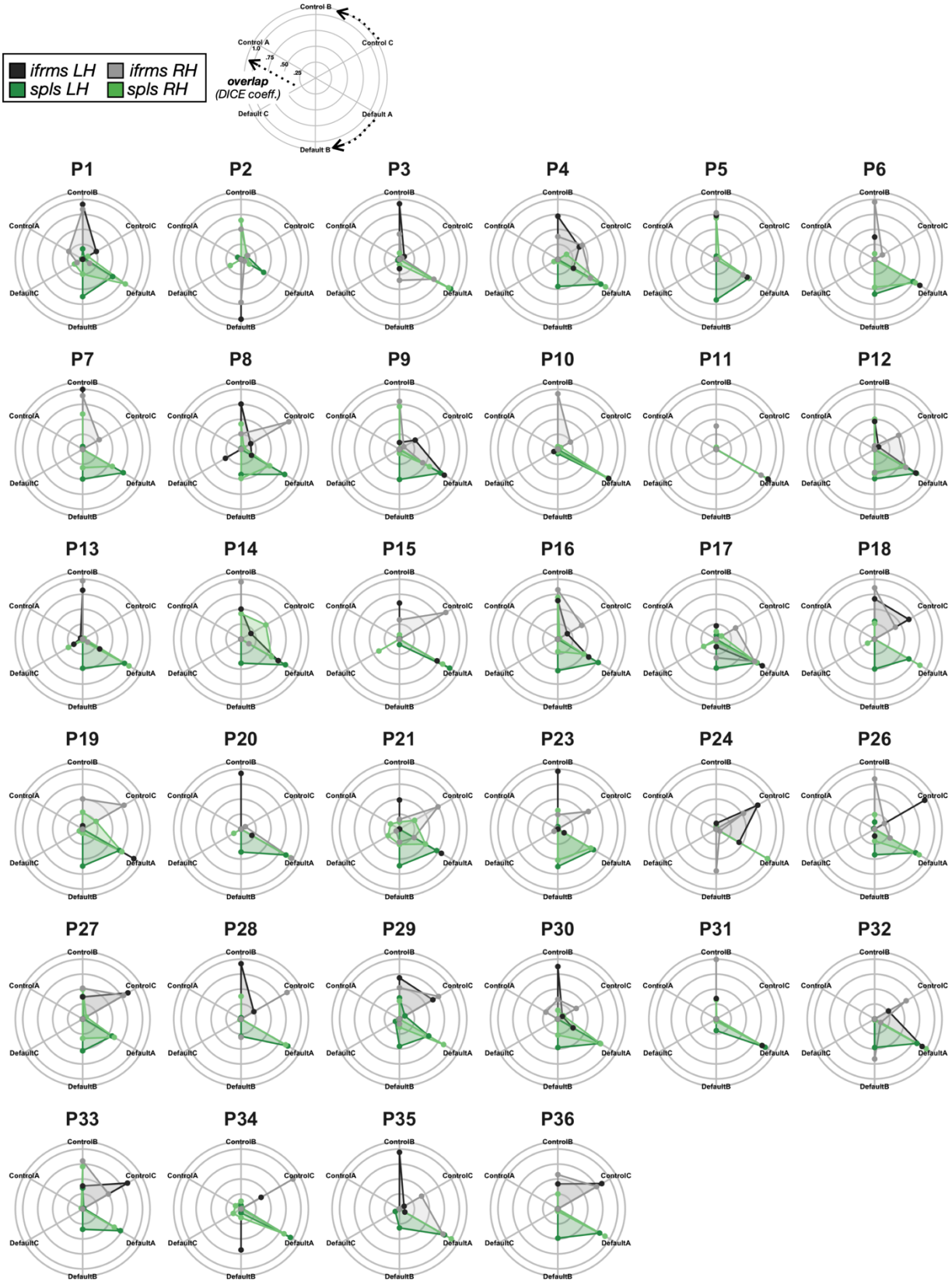
ifrms LH
ifrms RH
spls LH
spls RH
overlap
(DICE coeff.)
Control B
Control C
Control A
Default C
Default A
Default B
1.0
.75
.50
.25
P1
P2
P3
P4
P5
P6
P7
P8
P9
P10
P11
P12
P13
P14
P15
P16
P17
P18
P19
P20
P21
P23
P24
P26
P27
P28
P29
P30
P31
P32
P33
P34
P35
P36
ControlB
ControlA
ControlC
DefaultC
DefaultA
DefaultB

Figure S10. Individual participant connectivity fingerprints of the *ifrms* and *spls* in the replication sample. Same layout as Figure S8, but for each individual in the replication sample. Note that two participants were excluded (P22 and P25) due to not having resting-state parcellations available.

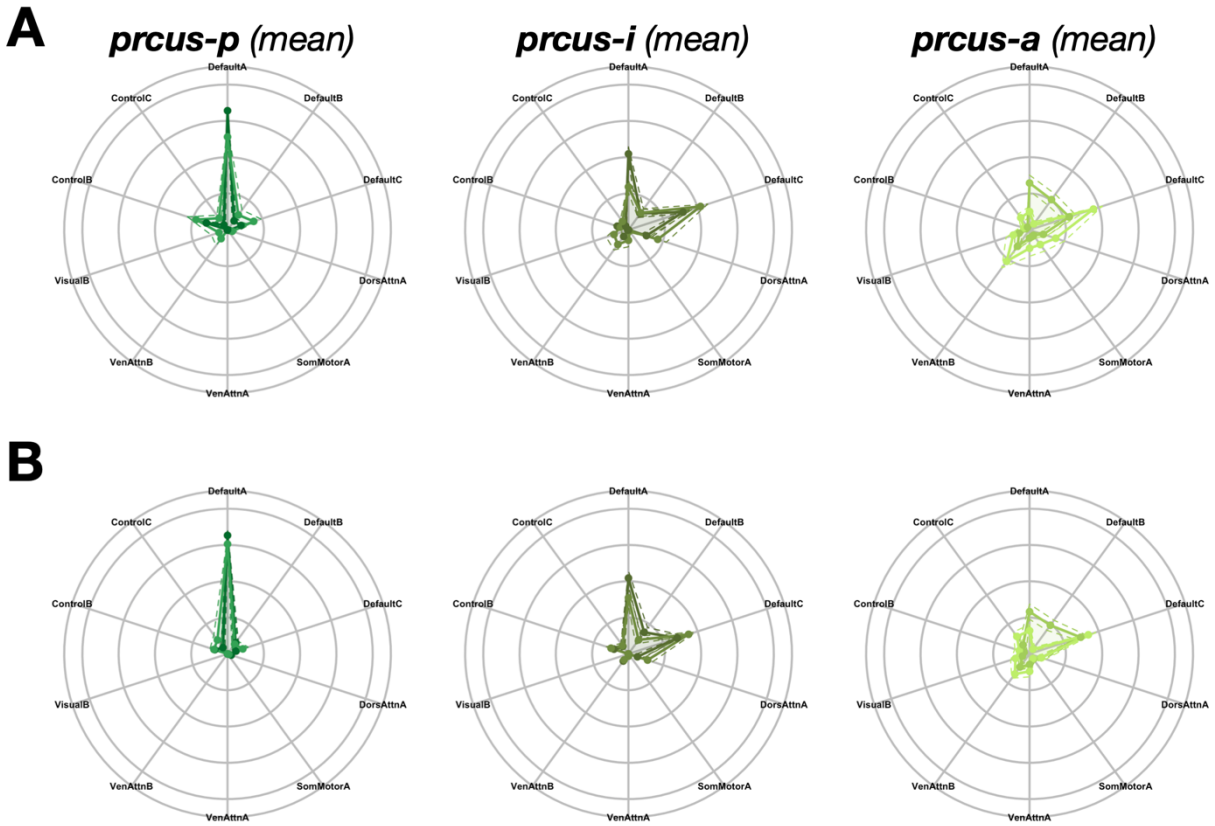

Figure S11. The three *prcus* sulci have different connectivity fingerprints. A. The mean connectivity fingerprints of the three *prcus* sulci in the discovery sample. Polar plots visualize the mean connectivity fingerprint of the three *prcus* sulci (posterior to anterior) for both hemispheres. The polar plots follow the same layout as Figure 5B. The solid-colored lines connect the means, and the dashed colored lines indicate ±1 SEm. Each *prcus* component is colored according to the legend in Figure 2A, with the darker shades indicating the left hemisphere (LH) and lighter shades indicating the right hemisphere (RH). **B.** The same layout as A, but for the replication sample.

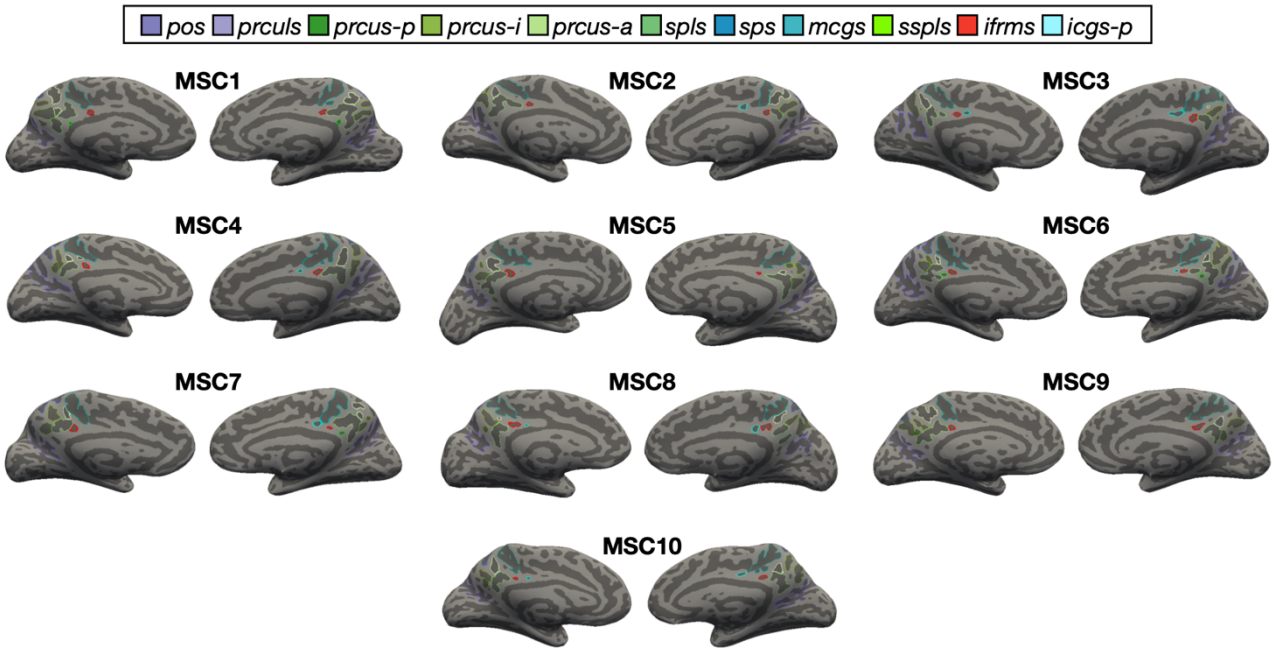

Figure S12. Manual PMC sulcal labels in the left and right hemispheres of each participant in the midnight scan club dataset. Same layout as Figure S4, but for the 10 midnight scan club participants (https://openneuro.org/datasets/ds000224/versions/1.0.3) (*43*).

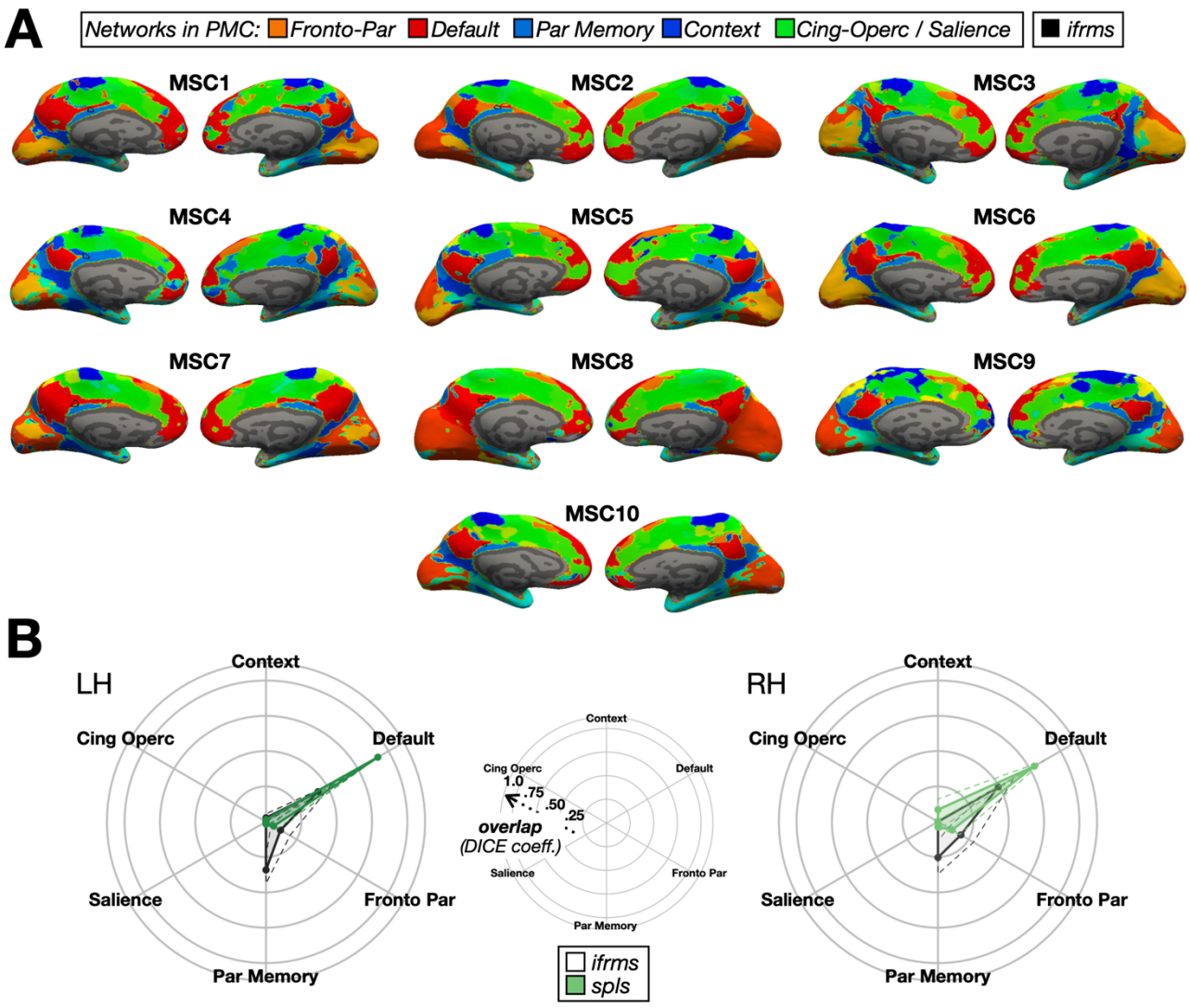

Figure S13. **The *ifrms* as a functional landmark: the MSC dataset. A.** Cortical reconstructions for each participant in the midnight scan club (N =10) (*43*) showing the *ifrms* (black outline) and resting-state functional connectivity parcellations. The key shows the relevant networks that are situated in the vicinity of the PMC. **B.** Polar plots showing the mean connectivity fingerprints of the *ifrms* and *spls* in the left hemisphere (LH, left, darker shades) and right hemisphere (RH, right, lighter shades) of the MSC sample. Solid lines: mean. Dashed lines: ±1 sem. Center: Legend for interpreting the polar plots in the left and right images. The closer to the periphery of the circle, the higher the Dice coefficient. Replicating the findings with the parcellation by Kong and colleagues (*42*), the *ifrms* has a distinguishable connectivity fingerprint from the *spls*—aligning more so with the parietal memory network than the *spls* and less so with the default network than the *spls*.

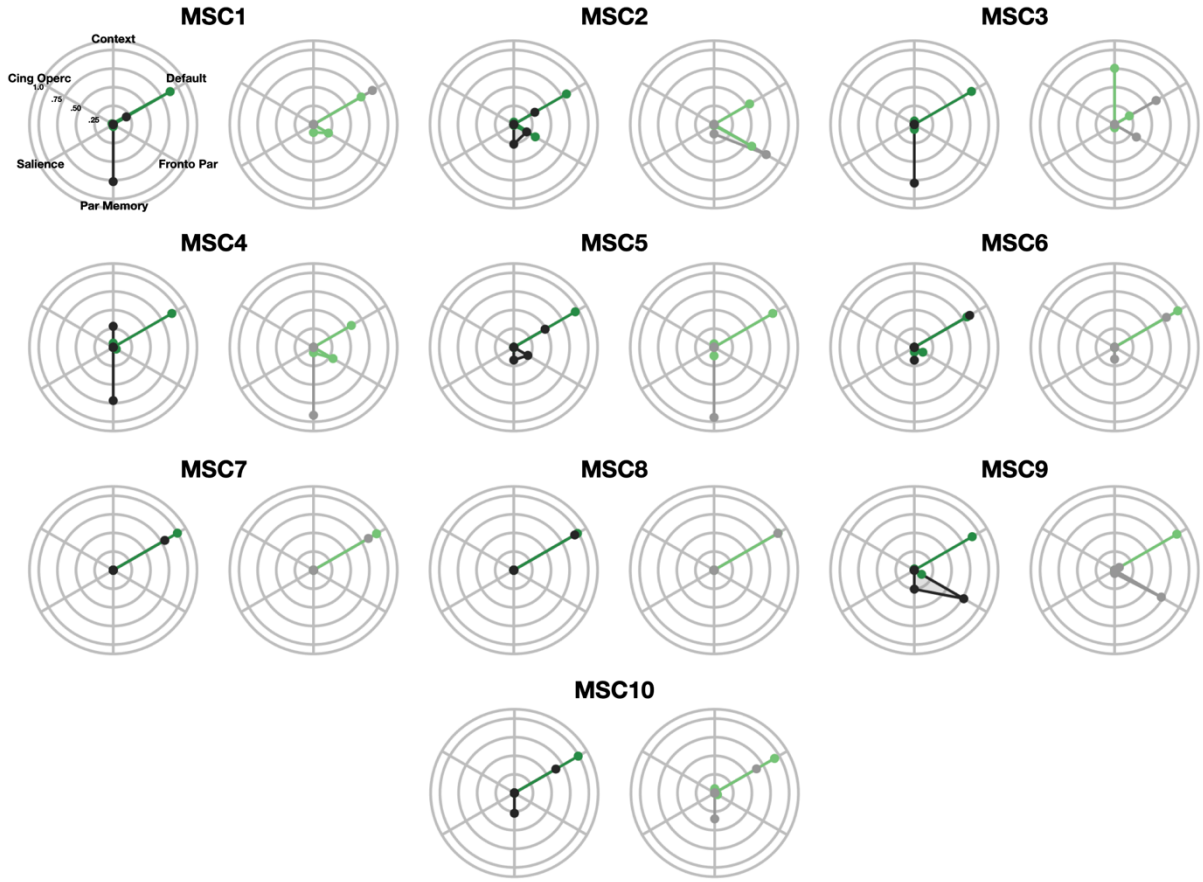

Figure S14. Individual connectivity fingerprints for the midnight scan club participants. Polar plots representing the connectivity fingerprints of the *ifrms* and *spls* in the left hemisphere (LH, left, darker shades) and right hemisphere (RH, right, lighter shades) of each participant in the MSC sample. Format is the same as in Figure S8.

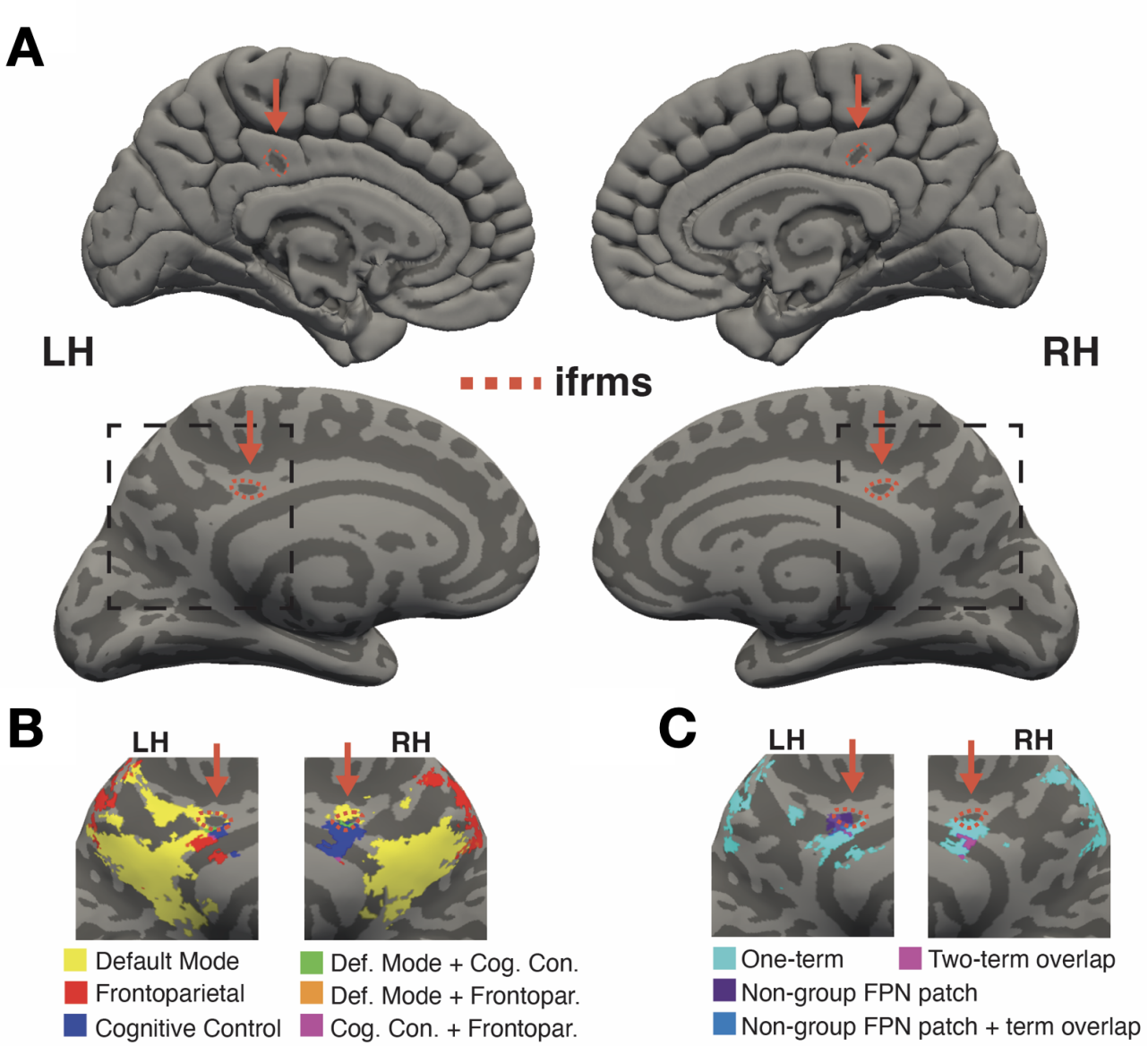

Figure S15. The *ifrms* as a functional landmark in over 1000 studies. A. Top: Pial surface of the MNI2009b atlas. The green dashed line indicates the location of the *ifrms* in this standard space atlas. Bottom: Inflated surface of the MNI2009b atlas. The green line indicates the location of the ifrms, and the yellow box indicates the posteromedial cortex (PMC) highlighted in B. **B.** Overlap visualization of whole brain, fdr-corrected ($p < 0.01$) association-test meta-analysis z-score maps of 'frontoparietal', 'cognitive control', and 'default mode' terms were downloaded from Neurosynth (https://neurosynth.org/) (*40*). These maps were generated from a chi-sq test comparing the proportion of studies demonstrating activation in a given voxel for studies containing the term of interest compared to all other studies in the database. Non-linear warping was used to align maps from the MNI152_2mm atlas to the MNI2009b atlas. Maps were then interpolated to the MNI2009b surface (using FreeSurfer's recon-all). **C.** The same process as B was used to visualize overlap maps of cognitive terms used synonymously to 'frontoparietal' (including: 'frontoparietal', 'cognitive control', 'demand' (proxy for demand network), 'executive', and 'domain general') (*45*). Light blue indicates above-threshold z-scores for one term, while yellow indicates above threshold z-scores were observed for at least two of the terms. There was no overlap of three or more terms in the PMC.

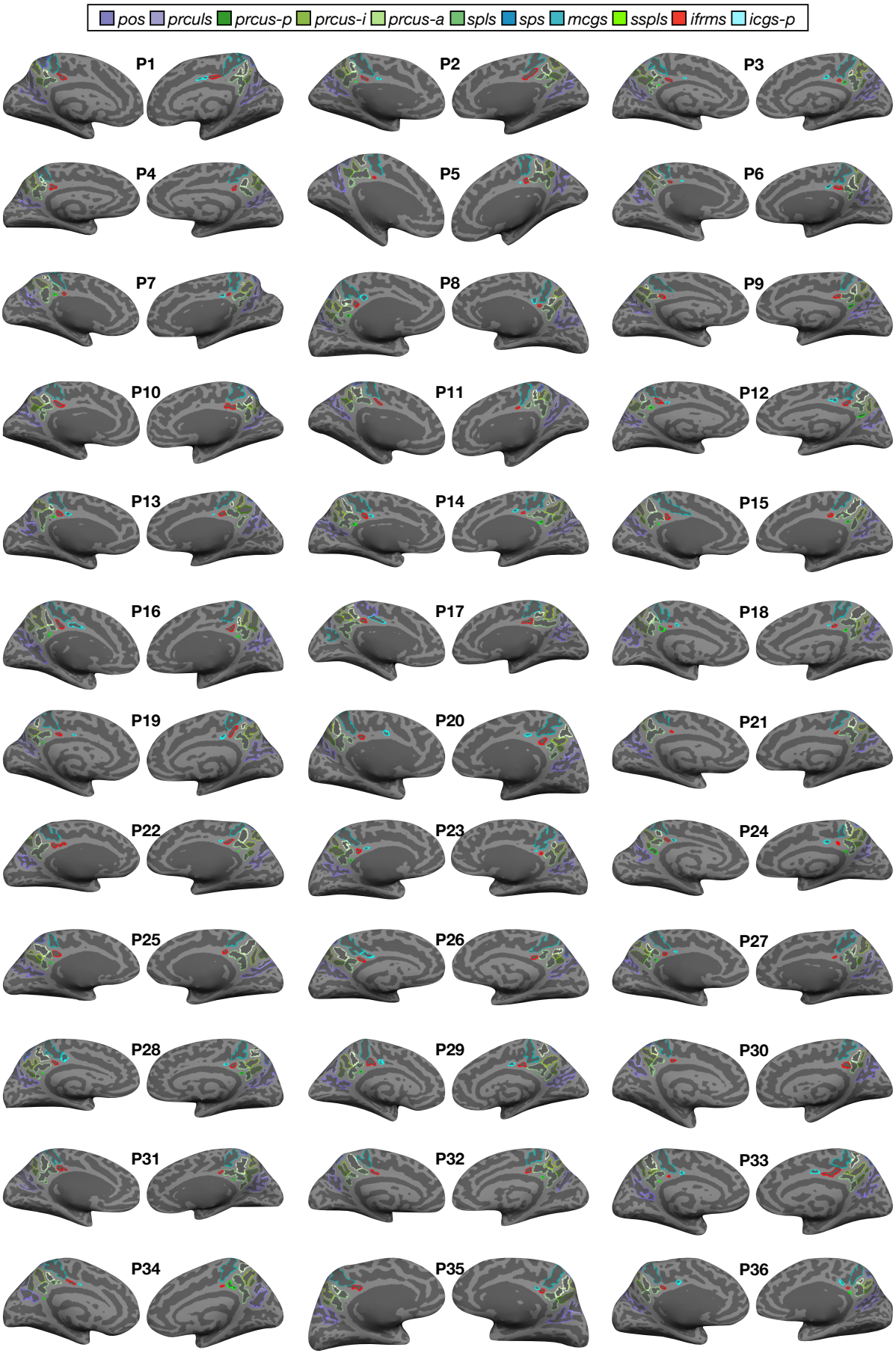
pos
prculs
prcus-p
prcus-i
prcus-a
spls
sps
mcgs
sspls
ifrms
icgs-p
P1
P2
P3
P4
P5
P6
P7
P8
P9
P10
P11
P12
P13
P14
P15
P16
P17
P18
P19
P20
P21
P22
P23
P24
P25
P26
P27
P28
P29
P30
P31
P32
P33
P34
P35
P36

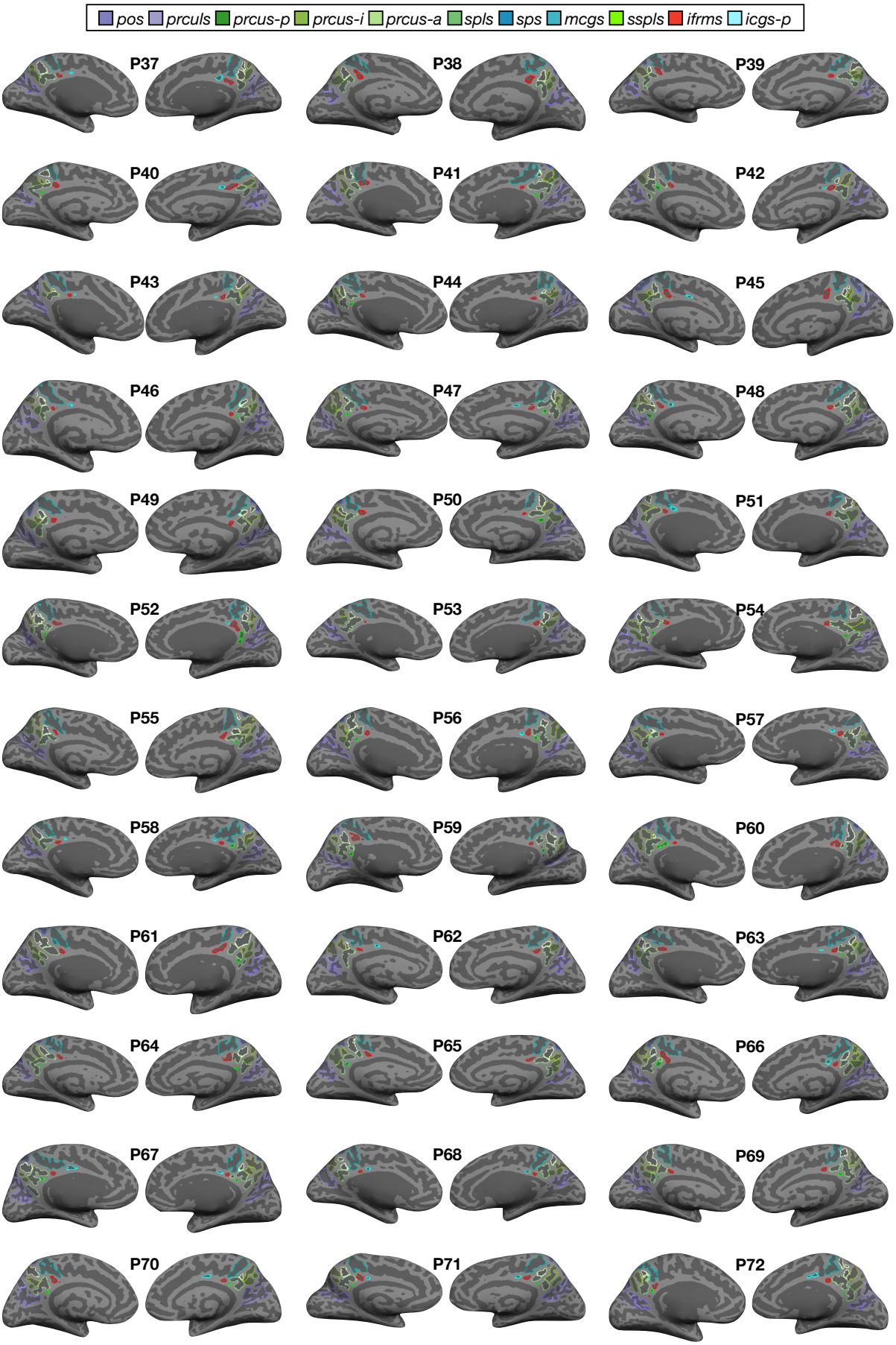
pos
prculs
prcus-p
prcus-i
prcus-a
spls
sps
mcgs
sspls
ifrms
icgs-p
P37
P38
P39
P40
P41
P42
P43
P44
P45
P46
P47
P48
P49
P50
P51
P52
P53
P54
P55
P56
P57
P58
P59
P60
P61
P62
P63
P64
P65
P66
P67
P68
P69
P70
P71
P72

Figure S16. Manual PMC sulcal labels in the left and right hemispheres of each human juvenile participant. Same layout as Figure S4, but for the human juvenile participants included in the present study.

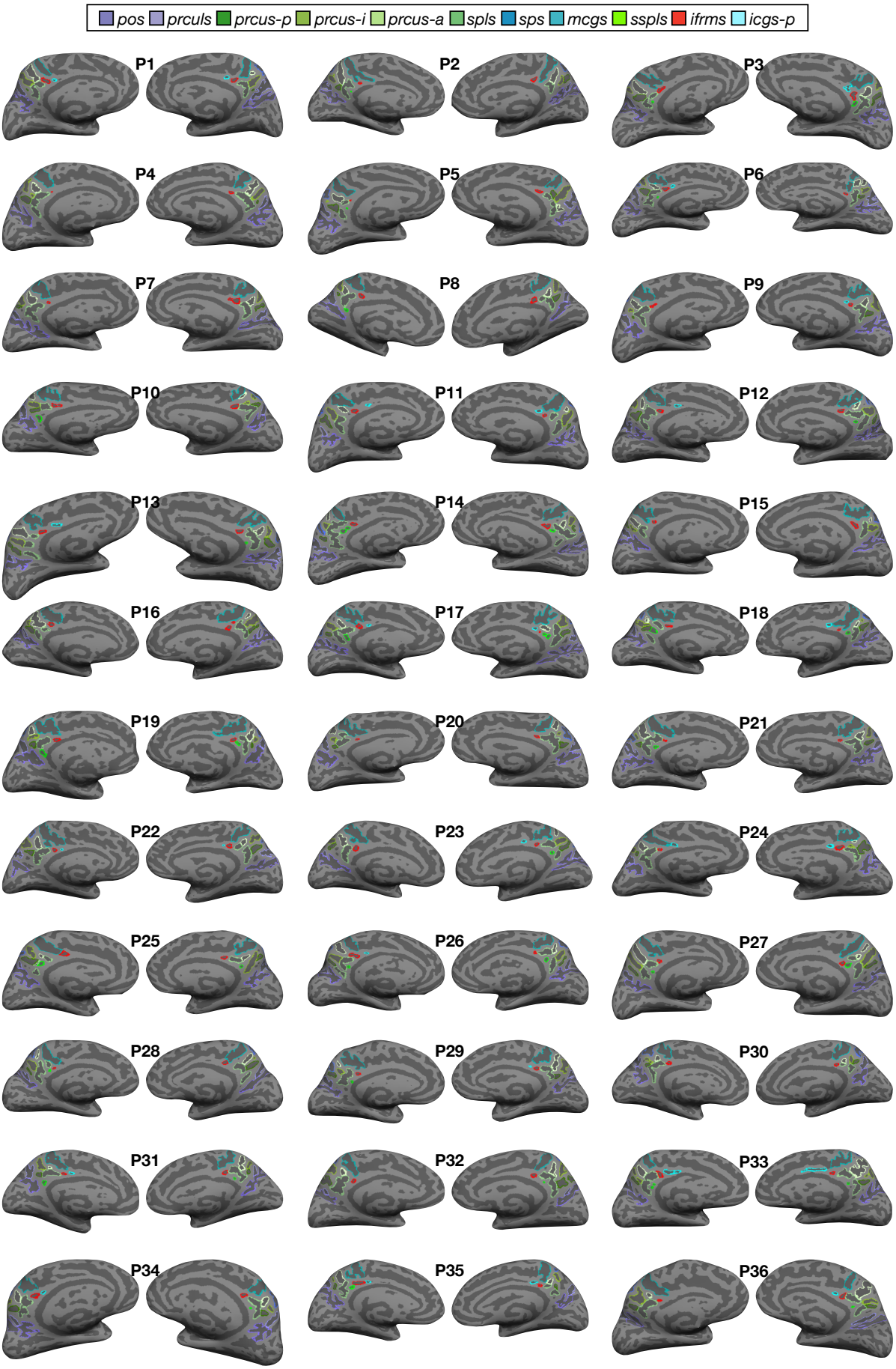
pos
prculs
prcus-p
prcus-i
prcus-a
spls
sps
mcgs
sspls
ifrms
icgs-p
P1
P2
P3
P4
P5
P6
P7
P8
P9
P10
P11
P12
P13
P14
P15
P16
P17
P18
P19
P20
P21
P22
P23
P24
P25
P26
P27
P28
P29
P30
P31
P32
P33
P34
P35
P36

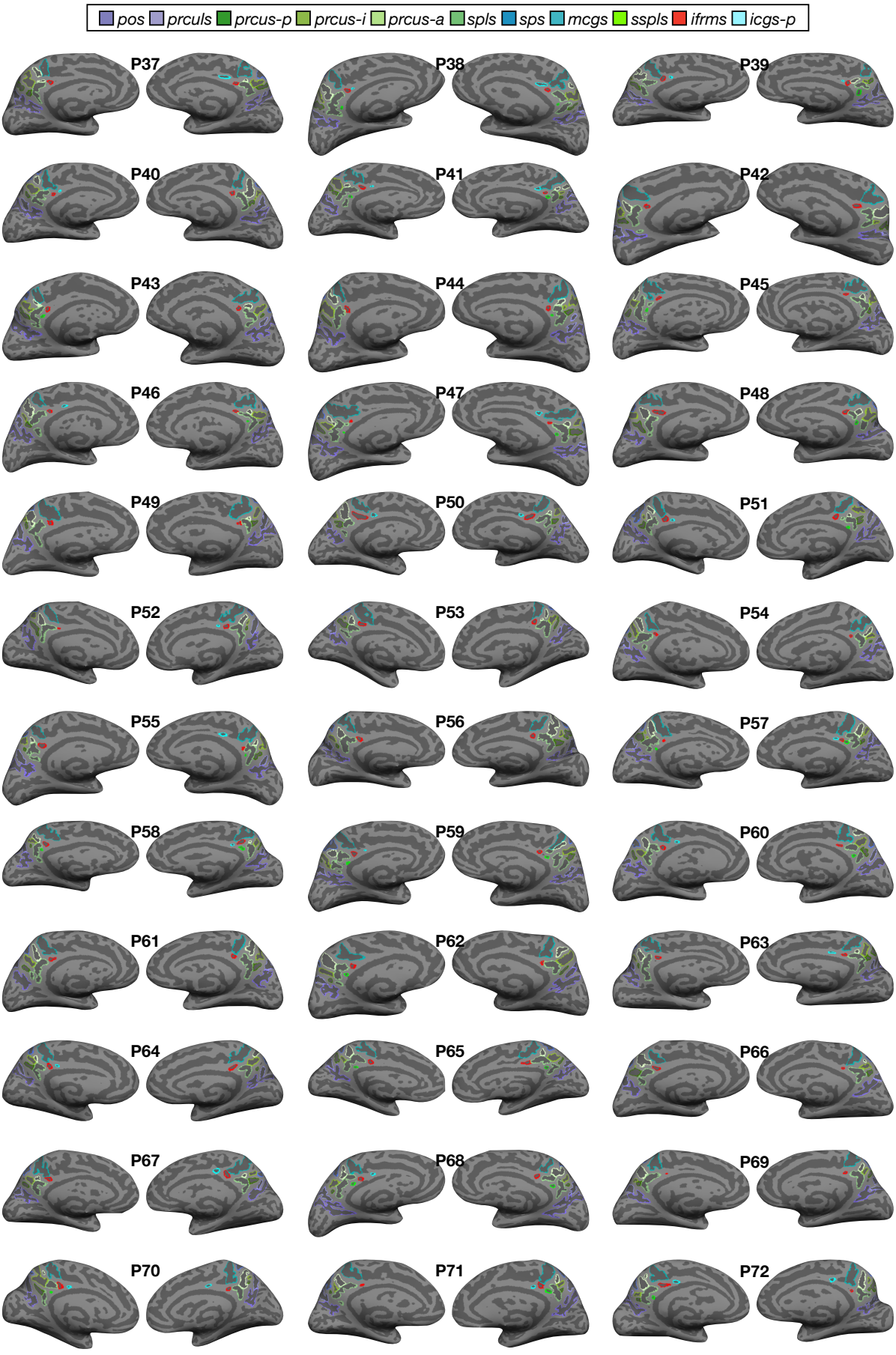
pos
prculs
prcus-p
prcus-i
prcus-a
spls
sps
mcgs
sspls
ifrms
icgs-p
P37
P38
P39
P40
P41
P42
P43
P44
P45
P46
P47
P48
P49
P50
P51
P52
P53
P54
P55
P56
P57
P58
P59
P60
P61
P62
P63
P64
P65
P66
P67
P68
P69
P70
P71
P72

Figure S17. Manual PMC sulcal labels in the left and right hemispheres of each human elderly participant. Same layout as Figure S4, but for the human elderly participants included in the present study.

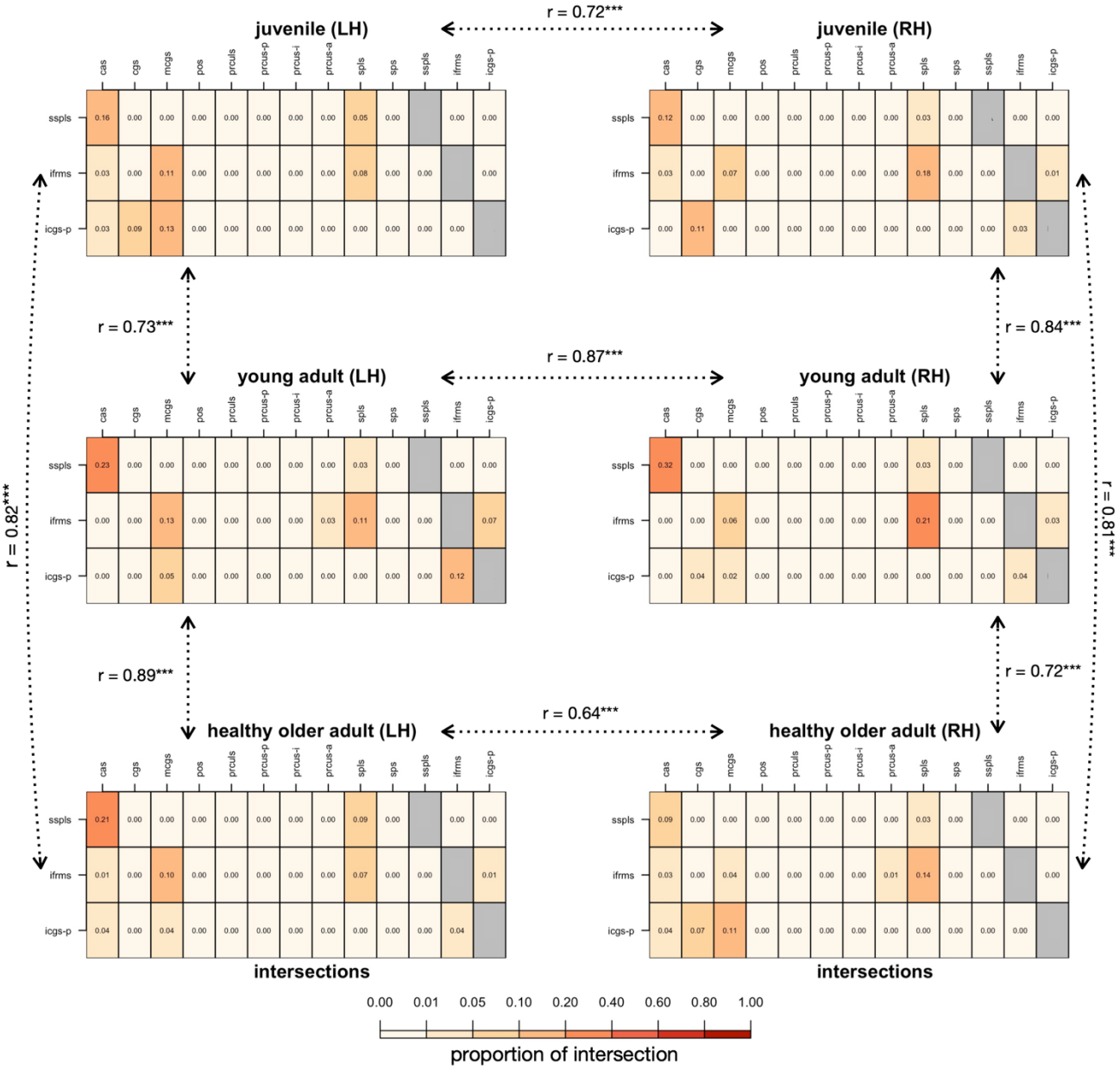

Figure S18. The sulcal patterns of shallow PCC sulci are similar between hemispheres and age groups. Same format as Figure S3. For each shallow PCC sulcus (*sspls, ifrms, icgs-p*), we report the proportion of intersection (frequency of occurrence/total number of observations) with each PMC sulcus for each age group (juvenile, young adult, healthy older adult). Note that the callosal sulcus (*cas*) and cingulate sulcus (*cgs*) were also included as the *sspls* intersected with the *cas* and the *icgs-p* intersected with the *cgs* frequently. Calculating the correlation between matrices shows that the intersections of these sulci is comparable (all *r*s > .60; all *p*s < 0.001) between hemispheres and age groups. The three most prevalent types for each shallow sulcus in the juvenile and healthy older adult samples are included in Tables S12 and S14, respectively.

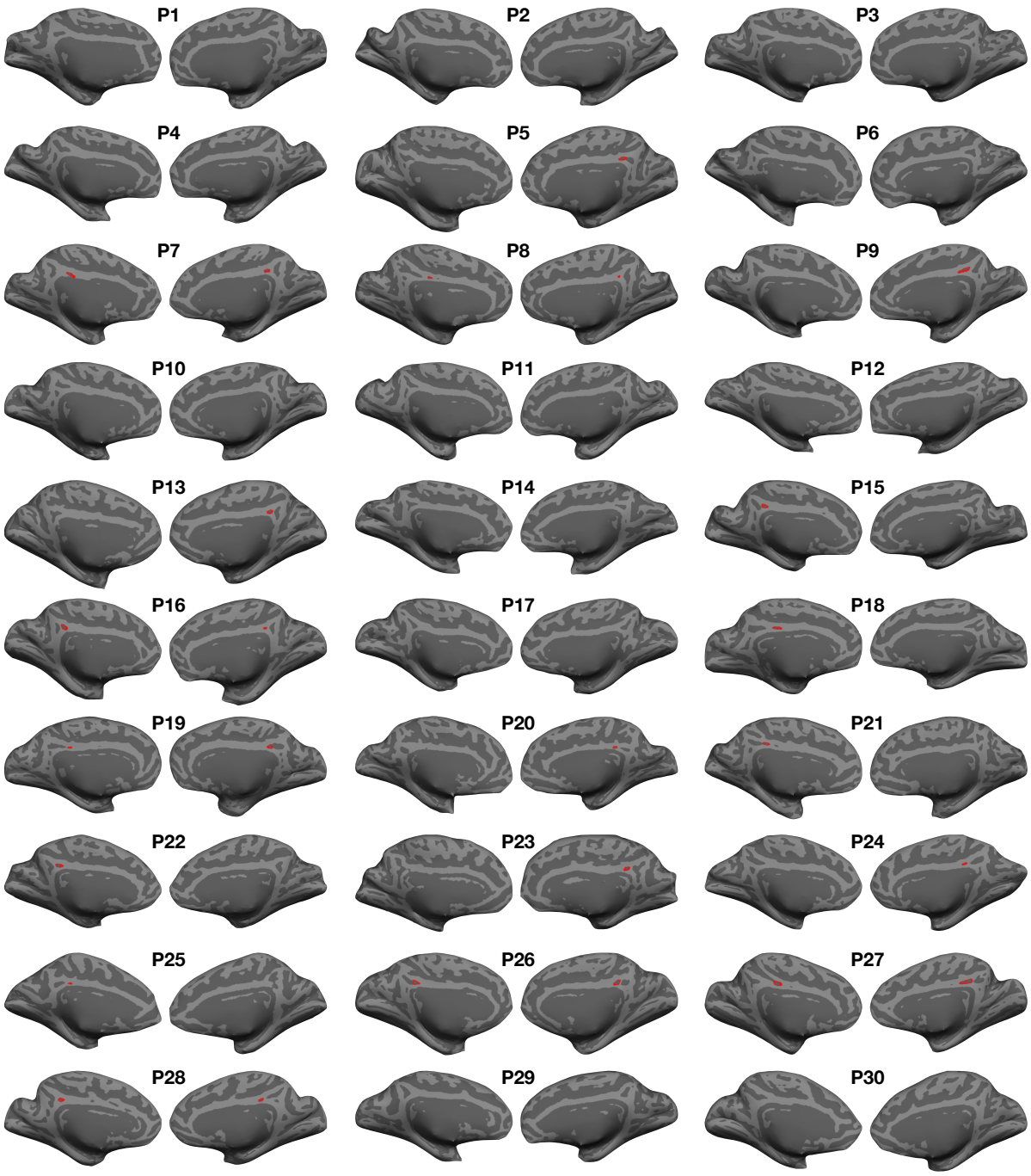
P1
P2
P3
P4
P5
P6
P7
P8
P9
P10
P11
P12
P13
P14
P15
P16
P17
P18
P19
P20
P21
P22
P23
P24
P25
P26
P27
P28
P29
P30

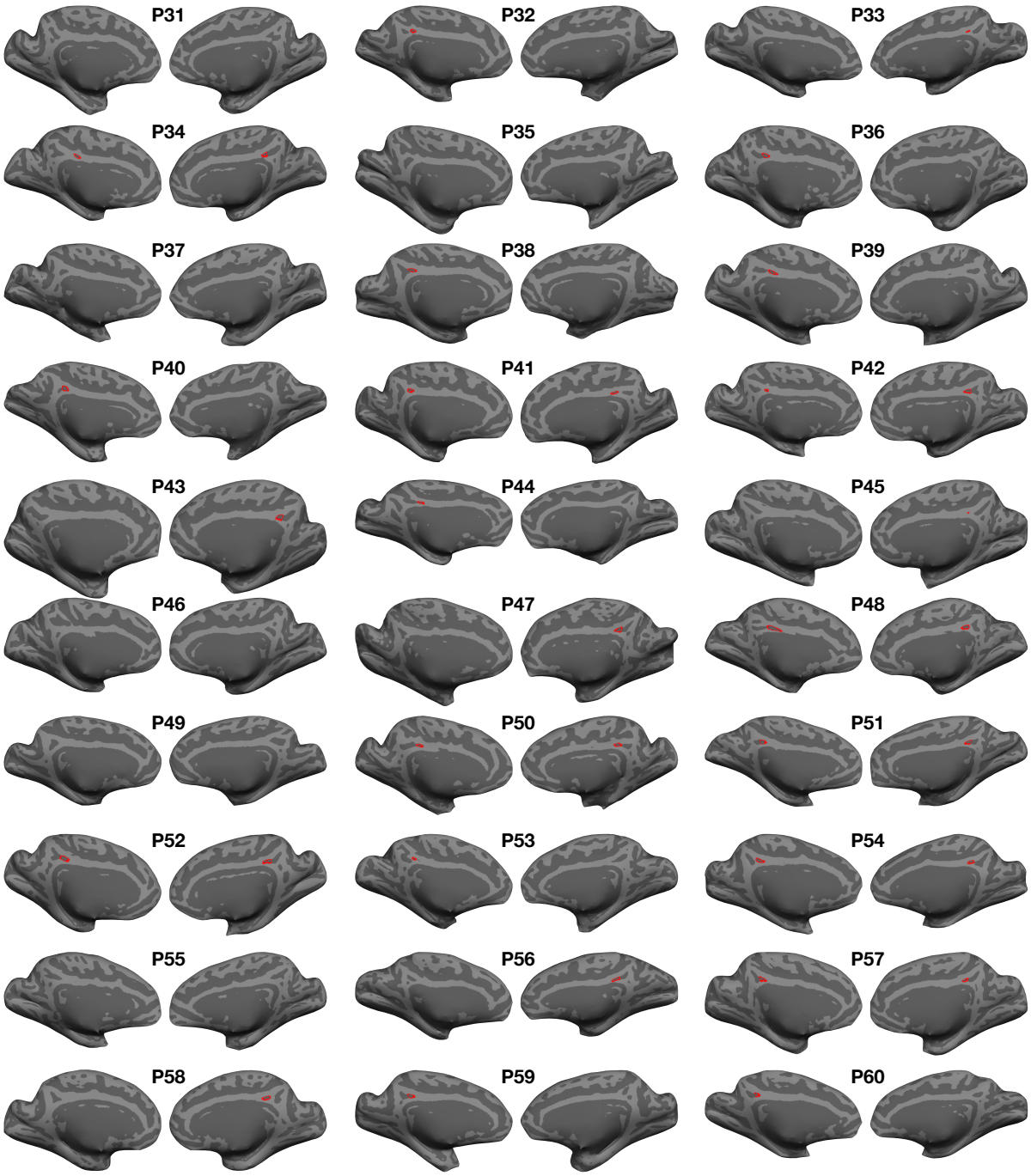

Figure S19. Manual *ifrms* labels in the left and right hemispheres in chimpanzees. Same layout as Figure S4, but for each chimpanzee included in the present study. Unlike the human participants, we only labeled the *ifrms* (not all PMC sulci) when it was identifiable.

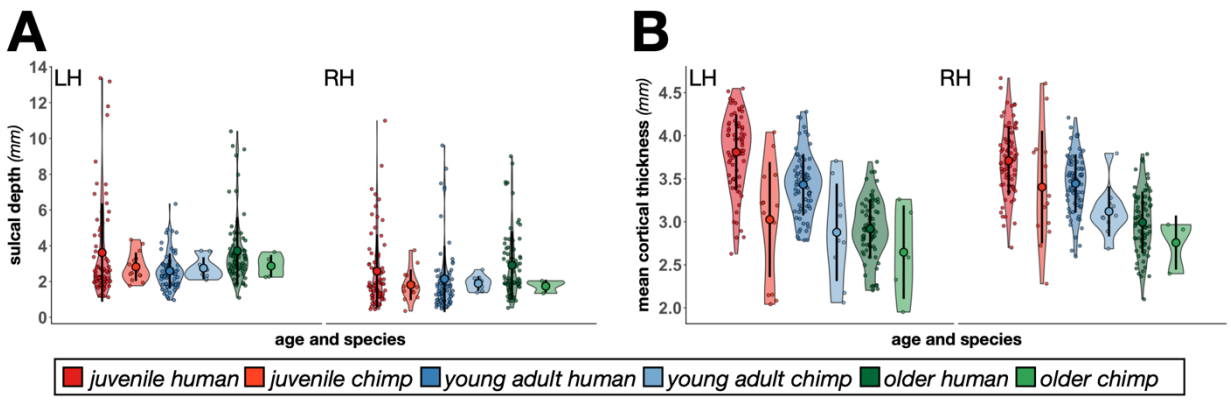

Figure S20. The morphological trends of the *ifrms* across age and species are the same regardless of normalization. A. Same layout as Figure 7C. Raw sulcal depth of the *ifrms,* calculated using a recent algorithm (*75*), across the lifespan and between species plotted for each individual participant in each hemisphere. The mean (large colored circles), standard deviation (black line), and kernel density estimate (colored "violin") are also plotted for each sulcus. There are also significant differences in raw depth of the *ifrms* between species and age groups as we found with normalized depth (Fig. 7C). **B.** Same layout as Figure 7D, but for raw cortical thickness (mm). The *ifrms* shows an age- and species-related decrease in raw cortical thickness as for normalized cortical thickness (Fig. 7D).

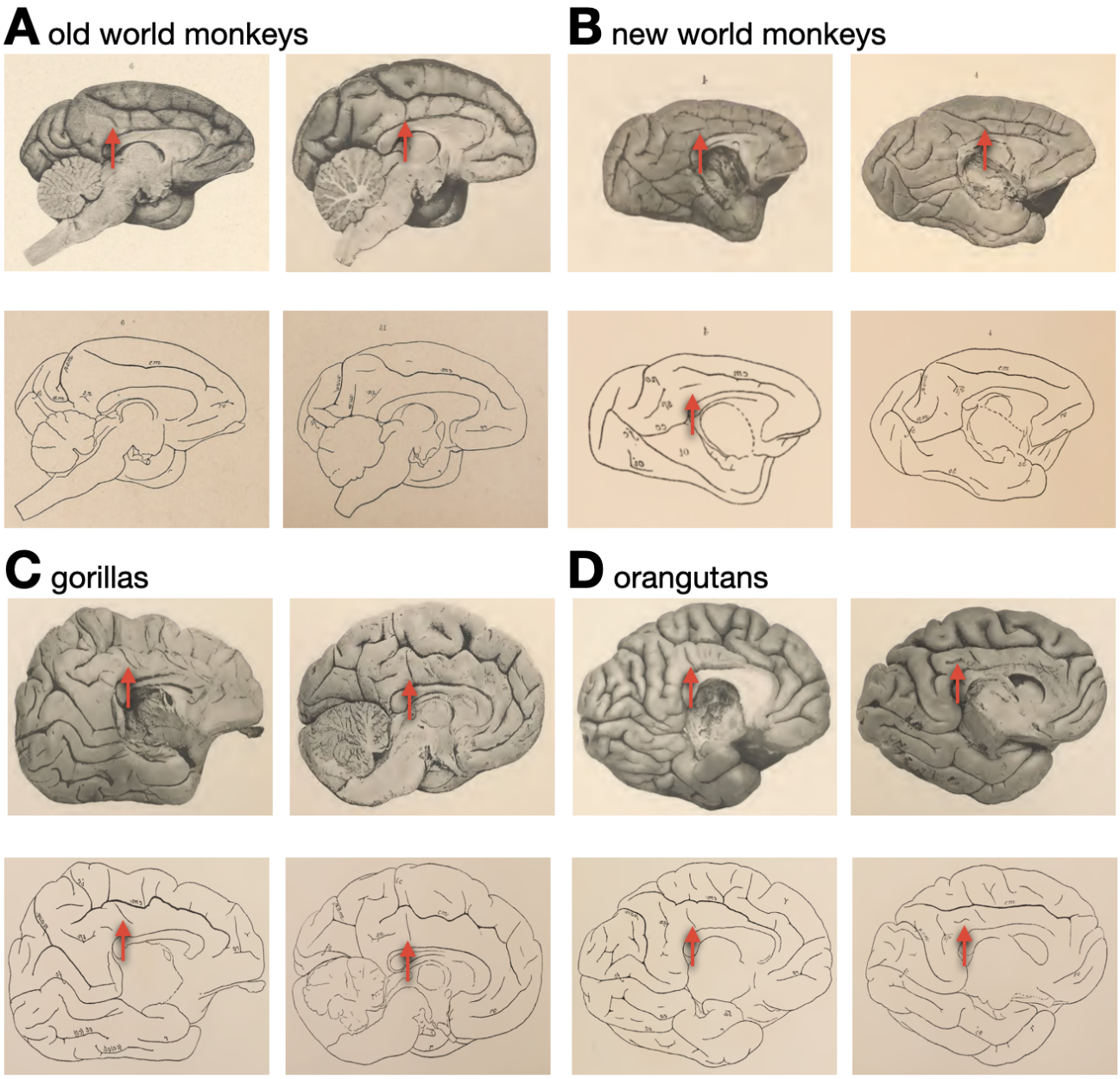

Figure S21. The *ifrms:* From dimple to sulcus across evolution? A. Top: A shallow dimple (*ifrmd*; red arrow) is identifiable underneath the *mcgs* in Old World monkeys. Bottom: Schematic illustration of the sulcal patterning provided by Retzius (*81*). Note that a shallow dimple is present underneath the *mcgs* in each photograph (red arrow), but not included in the schematic illustration. **B.** Same as A, but for New World monkeys. Bottom left: Note that Retzius does include an unlabeled indentation in his schematic (red arrow). **C.** The *ifrms* labeled in two example gorilla hemispheres. **D.** The *ifrms* labeled in two example orangutan hemispheres. Overall, a shallow indentation (dimple) located underneath the *mcgs* was present in 63.83% (30/47) and 40% (4/10) of New World monkey and Old World monkey hemispheres, respectively. A sulcal indentation underneath the *mcgs* was identifiable in 75% (3/4) of gorilla and 75% (6/8) of orangutan hemispheres present in Retzius' atlas. Not pictured: the *ifrms* was identifiable in 83.33% (15/18) of chimpanzee hemispheres in the atlas. All post-mortem hemispheres inspected from Retzius (*81*) will be included on our lab website with the

publication of this paper. Broadly speaking, the culmination of these data support the idea that cortical indentations beneath the *mcgs* are shallow dimples (the *ifrmd*) in old World and New World monkeys, which then deepen and become a tertiary sulcus (the *ifrms*) in human and non-human hominoids.

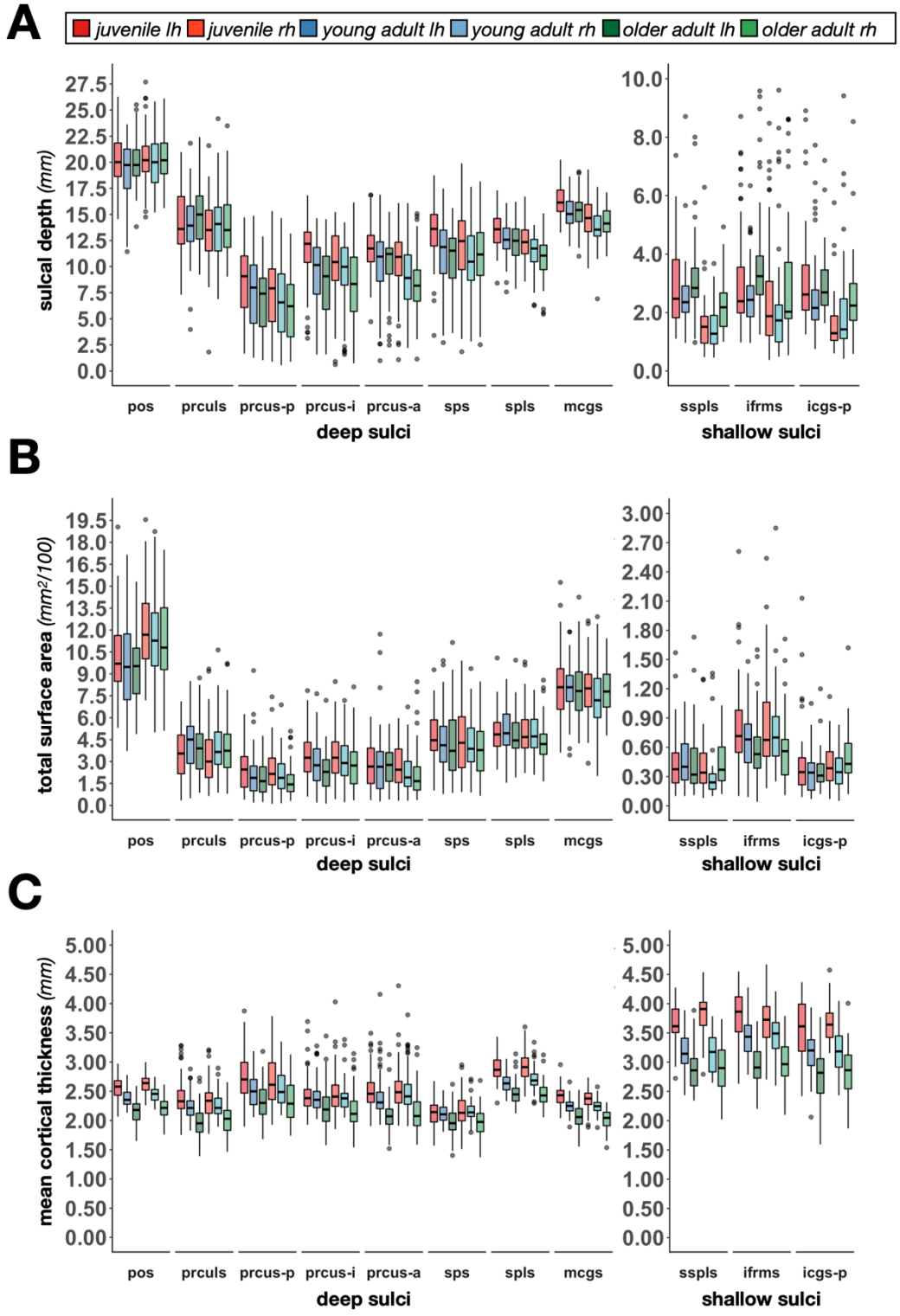

Figure S22. Morphological features of PMC sulci across age groups in humans. A. Sulcal depth (mm) of all 11 PMC sulci across the three age groups (juvenile, young adult, and healthy older adult) and hemispheres. The measures of central tendency for each sulcus are visualized with a box plot (outliers

shown as dark gray circles). Sulci are ordered posterior to anterior along the x-axis and separated into deep and shallow sulci to appreciate the range of values for the shallower sulci. Each age group and hemisphere combination are colored according to the legend. **B.** Same as A but for total surface area (mm^2). Note that these values are scaled by a factor of 100. **C.** Same as A but for mean cortical thickness (mm). The mean and standard deviation values are also provided in Tables S15- S17.

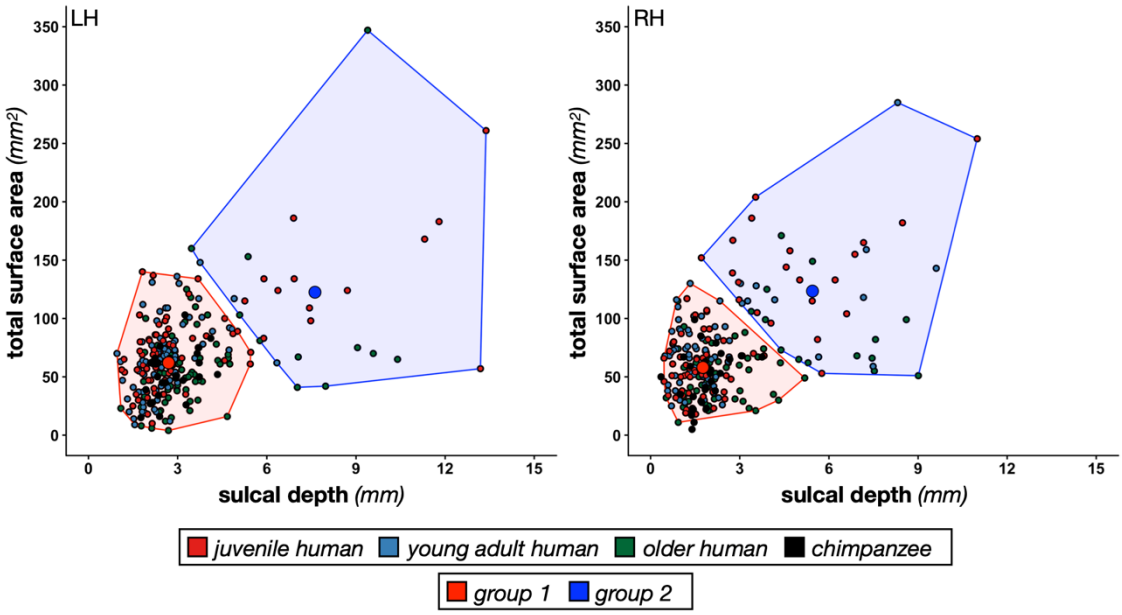

Figure S23. Quantitatively classifying the *ifrms* based on morphology (depth and surface area). Cluster plots visualizing the results of using k-means clustering on the depth and surface area of the *ifrms* in both hemispheres. Individual participants (small dots) are colored by their age group (for humans) or species (for chimpanzees; top key). The *ifrms* clustered into two groups (group 1, red; group 2, blue; bottom key) in both the left (LH) and right hemispheres (RH). The group centers are the large red/blue dots. It was more common for an *ifrms* to be in group 1 (LH: 217/244; RH: 197/243) than group 2 (LH: 27/244; RH: 46/243). The *ifrms* in group 1 is shallower and smaller (group centers; LH: depth = 2.71, surface area = 60.82; RH: depth = 1.76, surface area = 56.87) than the *ifrms* in group 2 (group centers; LH: depth = 7.62, surface area = 122.48; RH: depth = 5.44, surface area = 121.85). Akin to previous work classifying tertiary sulci (for example see (*15, 16, 19, 54*), these groupings differentiate a "present" *ifrms* from a "prominent" *ifrms*, respectively. Interestingly, all chimpanzee *ifrms* fall within the "present" group in both hemispheres (see the black points). Future work should seek to relate these classifications of the *ifrms*, as well as the presence/absence of the chimpanzee *ifrms,* to cognitive abilities and disorders.

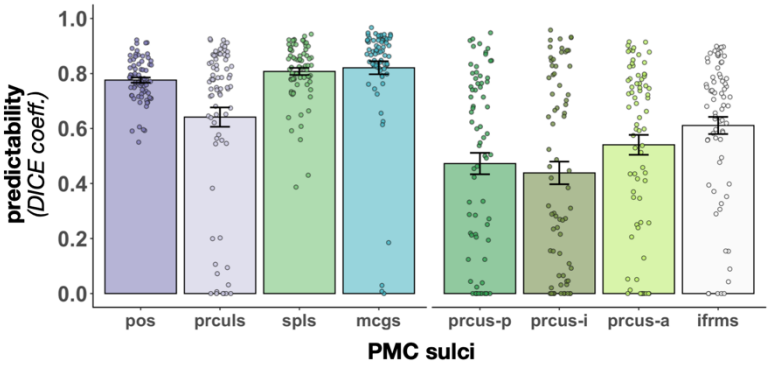

Figure S24. Automatically defining PMC sulci using deep learning algorithms. Overlap (DICE coefficient) between predicted and manual location of PMC sulci that are identifiable in every young adult hemisphere for spherical convolutional and context aware training (Methods) (*56*). Bars represent average values, and the error bars indicate ±1 SEm. Circles represent each individual. Large, deep sulci are positioned to the left of the x-axis, while smaller, shallower sulci are positioned to the right. Predictability for the latter is lower than the former. However, predictability of the *ifrms* is higher than the three larger precuneal sulci (see Results).

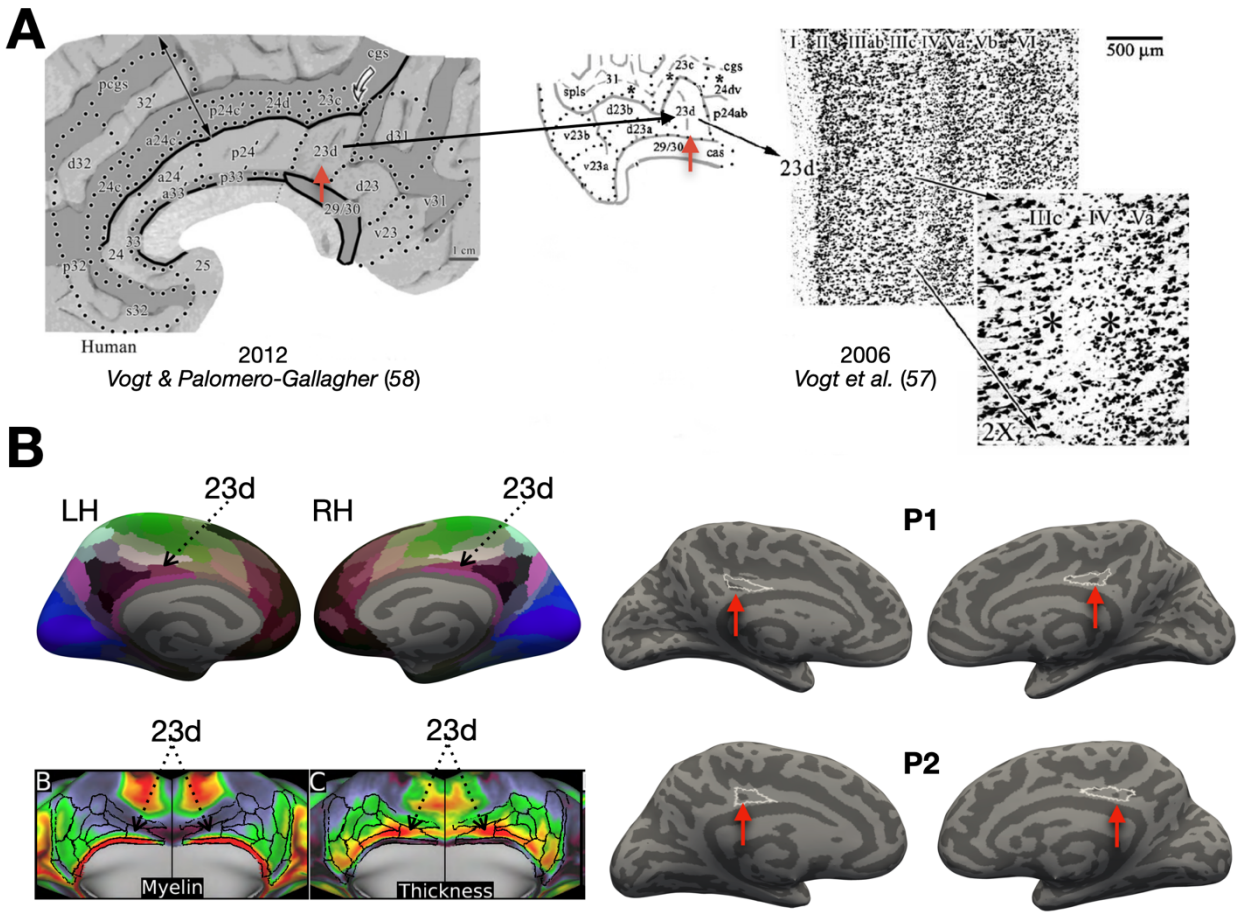

Figure S25. **The *ifrms* is a potential cytoarchitectonic and multimodal landmark. A.** The *ifrms* (red arrow) is located within area 23d, which is dysgranular (as shown by its small layer IV in the inset by Vogt *et al.* (*57*)). **B.** Left, top: area 23d is defined in the multimodal parcellation by Glasser and colleagues (*44*) which is visualized here on the fsaverage cortical surface in magenta (black arrows) in both the left (LH) and right hemisphere (RH). Left, bottom: Like the *ifrms*, area 23d is lightly myelinated (left, green) and cortically thick (right, red), two features which differentiate it from surrounding areas at the group level. Right: The outline of area 23d (in white) defined in the group map projected to two randomly chosen individual participants in both hemispheres. The *ifrms* in individual participants is located within area 23d based on multimodal features at the group level. These observations tentatively identify the *ifrms* as a sulcal landmark based on cytoarchitectonic and multimodal features, which can be tested in individual participants in future studies.

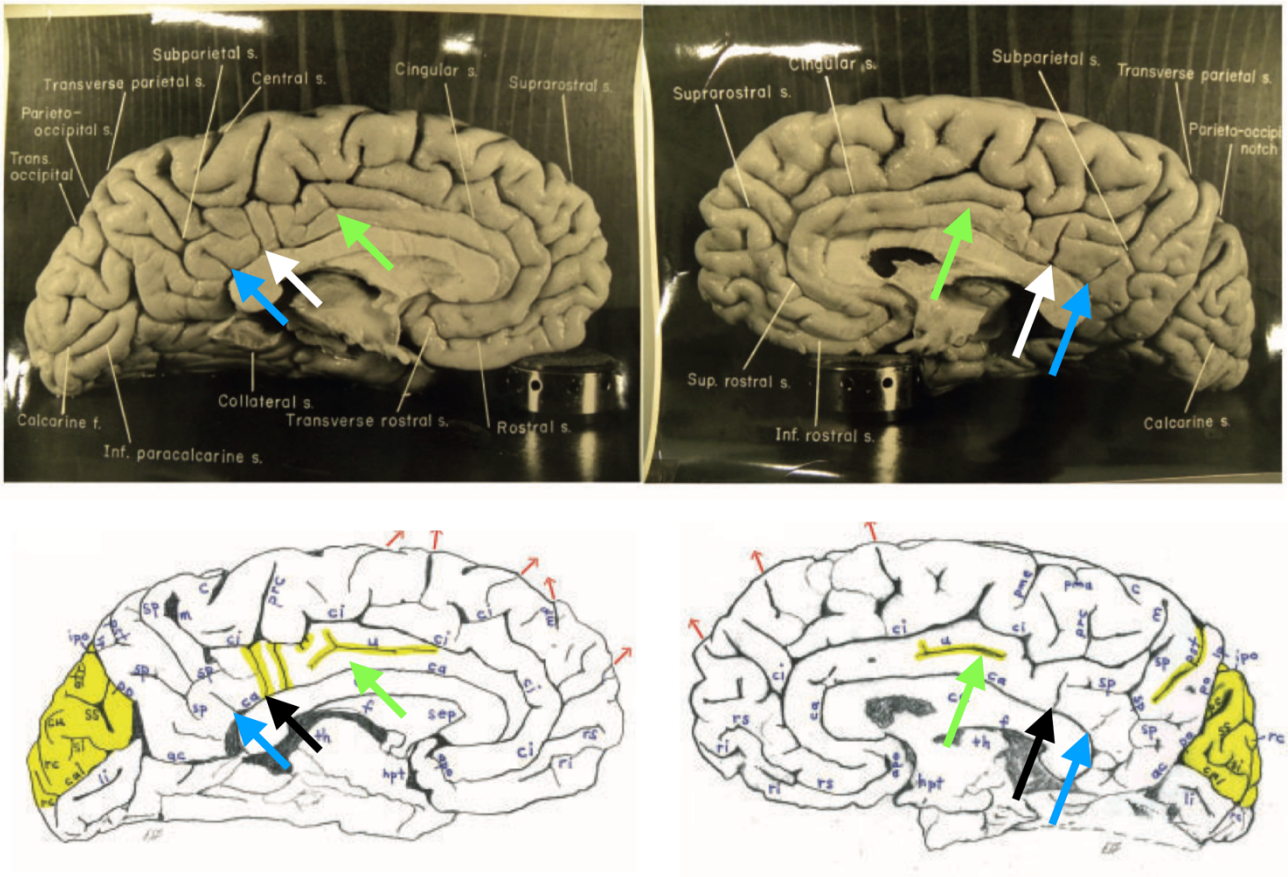

Figure S26. Even Einstein had an *ifrms*. Top: Photographs of Einstein's brain. Blue arrow: *sspls*. White/Black arrow: *ifrms*. Green arrow: intracingulate sulcus as identified by Borne and colleagues (*47*). Bottom: Schematic illustration highlighting (in yellow) differences in the sulcal patterning in Einstein's brain compared to typical sulcal patterning (from Falk *et al.* (*91*)). We highlight that the *ifrms*, and nearby shallow sulci, examined in the present study, are identified as abnormal in Einstein's brain. This highlights the necessity to identify all sulci and dimples of the cerebral cortex in order to accurately assess typicality and atypicality, as well as how individual differences in sulcal patterning relate to function, anatomy, and cognition in both typical and atypical brains. In this particular case, the omission of the *ifrms* and other "tiny" or shallow sulci in PCC resulted in the inaccurate conclusion that this was a special feature of Einstein's brain. Instead, this sulcal patterning in Einstein's PCC is actually common in humans and also present in many chimpanzee brains as we quantify in the present paper.

Supplementary Tables

sulci	appearance in LH	LH %	appearance in RH	RH %
pos	36/36	100.00	36/36	100.00
prculs	36/36	100.00	36/36	100.00
prcus-p	36/36	100.00	36/36	100.00
prcus-i	36/36	100.00	36/36	100.00
prcus-a	36/36	100.00	36/36	100.00
spls	36/36	100.00	36/36	100.00
sps	35/36	97.22	34/36	94.44
mcgs	36/36	100.00	36/36	100.00
sspls	23/36	63.89	18/36	50.00
ifrms	36/36	100.00	36/36	100.00
icgs-p	19/36	52.78	23/36	63.89

Table S1. Incidence rates of PMC sulci in the discovery sample. This table illustrates the incidence rates of the 8-11 definable PMC sulci in the discovery young adult sample (N = 36 participants). The incidence rate of each sulcus (posterior to anterior) is provided in number and percent for both the left (LH) and right hemispheres (RH). The abbreviations used are as follows: anterior precuneal sulcus (*prcus-a*); intermediate precuneal sulcus (*prcus-i*); inframarginal sulcus (*ifrms*); marginal ramus of the cingulate sulcus (*mcgs*); parieto-occipital sulcus (*pos*); posterior intracingulate sulcus (*icgs-p*); posterior precuneal sulcus (*prcus-p*); precuneal limiting sulcus (*prculs*); splenial sulcus (*spls*); subsplenial sulcus (*sspls*); superior parietal sulcus (*sps*).

sulci	appearance in LH	LH %	appearance in RH	RH %
pos	36/36	100.00	36/36	100.00
prculs	36/36	100.00	36/36	100.00
prcus-p	36/36	100.00	36/36	100.00
prcus-i	36/36	100.00	36/36	100.00
prcus-a	36/36	100.00	36/36	100.00
spls	36/36	100.00	36/36	100.00
sps	30/36	83.33	34/36	94.44
mcgs	36/36	100.00	36/36	100.00
sspls	17/36	47.22	20/36	55.56
ifrms	36/36	100.00	36/36	100.00
icgs-p	24/36	66.67	23/36	63.89

Table S2. Incidence rates of PMC sulci in the replication sample. This table illustrates the incidence rates of the 8-11 definable PMC sulci in the replication young adult sample (N = 36 participants). The incidence rate of each sulcus (posterior to anterior) is provided in number and percent for both the left (LH) and right hemispheres (RH). The abbreviations used are as follows: anterior precuneal sulcus (*prcus-a*); intermediate precuneal sulcus (*prcus-i*); inframarginal sulcus (*ifrms*); marginal ramus of the cingulate sulcus (*mcgs*); parieto-occipital sulcus (*pos*); posterior intracingulate sulcus (*icgs-p*); posterior precuneal sulcus (*prcus-p*); precuneal limiting sulcus (*prculs*); splenial sulcus (*spls*); subsplenial sulcus (*sspls*); superior parietal sulcus (*sps*).

Sulci	First	%	Second	%	Third	%
prcus-a						
LH (n=36)	*spls*	77.8	*prcus-i*	13.9	*free*	11.1
RH (n=36)	*spls*	58.3	*mcgs*	27.8	*prcus-i*	22.2
prcus-i						
LH (n=36)	*spls*	47.2	*free*	38.9	*prcus-p*	13.9
RH (n=36)	*spls*	61.1	*prcus-a*	22.2	*prcus-p*	13.9
prcus-p						
LH (n=36)	*spls*	55.6	*free*	36.1	*prcus-i*	13.9
RH (n=36)	*spls*	41.7	*free*	38.9	*prcus-i*	13.9

Table S3. Most common intersections of the discovery sample's precuneal sulci. This table illustrates the different sulcal patterns, or types, of the three precuneal sulci (*prcus*) identified in the discovery young adult sample (N = 36 participants). For each sulcus, the top three most prevalent sulcal patterns and their percent of occurrence are provided for both the left (LH) and right hemispheres (RH). The incidence of each sulcus in this sample is also provided for each hemisphere for reference. The abbreviations used are as follows: anterior precuneal sulcus *(prcus-a*); intermediate precuneal sulcus (*prcus-i*); marginal ramus of the cingulate sulcus (*mcgs*); no intersections (*free*); posterior precuneal sulcus (*prcus-p*); splenial sulcus (*spls*).

Sulci	First	%	Second	%	Third	%
icgs-p						
LH (n=19)	*free*	78.9	*ifrms*	15.8	*mcgs*	5.3
RH (n=23)	*free*	95.7	*mcgs*	4.3	---	0.0
ifrms						
LH (n=36)	*free*	83.3	*icgs-p*	8.3	*mcgs*	5.6
RH (n=36)	*free*	80.6	*spls*	16.7	*mcgs*	2.8
sspls						
LH (n=23)	*free*	73.9	*cas*	26.1	---	0.0
RH (n=18)	*free*	77.8	*cas*	22.2	---	0.0

Table S4. Most common intersections of the discovery sample's shallow PCC sulci. This table illustrates the different sulcal patterns, or types, of the three shallow PCC sulci identified in the discovery young adult sample (N = 36 participants). For each sulcus, the top three most prevalent sulcal patterns and their percent of occurrence are provided for both the left (LH) and right hemispheres (RH). The incidence of each sulcus in this sample is also provided for each hemisphere for reference. The abbreviations used are as follows: callosal sulcus (*cas*); inframarginal sulcus (*ifrms*); marginal ramus of the cingulate sulcus (*mcgs*); no intersections (*free*); no other option (---); posterior intracingulate sulcus (*icgs-p*); splenial sulcus (*spls*); subsplenial sulcus (*sspls*).

Sulci	First	%	Second	%	Third	%
prcus-a						
LH (n=36)	*spls*	83.3	*prcus-i*	22.2	*mcgs*	13.9
RH (n=36)	*spls*	72.2	*prcus-i*	19.4	*mcgs*	16.7
prcus-i						
LH (n=36)	*spls*	63.9	*prcus-a*	22.2	*free*	22.2
RH (n=36)	*spls*	63.9	*free*	25.0	*prcus-a*	19.4
prcus-p						
LH (n=36)	*spls*	55.6	*free*	33.3	*prcus-i*	13.9
RH (n=36)	*spls*	55.6	*free*	36.1	*prcus-i*	11.1

Table S5. Most common intersections of the replication sample's precuneal sulci. This table illustrates the different sulcal patterns, or types, of the three precuneal sulci (*prcus*) identified in the replication young adult sample (N = 36 participants). For each sulcus, the top three most prevalent sulcal patterns and their percent of occurrence are provided for both the left (LH) and right hemispheres (RH). The incidence of each sulcus in this sample is also provided for each hemisphere for reference. The abbreviations used are as follows: anterior precuneal sulcus (*prcus-a*); intermediate precuneal sulcus (*prcus-i*); marginal ramus of the cingulate sulcus (*mcgs*); no intersections (*free*); posterior precuneal sulcus (*prcus-p*); splenial sulcus (*spls*).

Sulci	First	%	Second	%	Third	%
icgs-p						
LH (n=24)	*free*	87.5	*ifrms*	8.3	*mcgs*	4.2
RH (n=23)	*free*	82.6	*ifrms*	8.7	*cgs*	8.7
ifrms						
LH (n=36)	*free*	66.7	*spls*	16.7	*mcgs*	11.1
RH (n=36)	*free*	61.1	*spls*	25.0	*mcgs*	8.3
sspls						
LH (n=17)	*free*	76.5	*cas*	17.6	*spls*	5.9
RH (n=20)	*free*	55.0	*cas*	40.0	*spls*	5.0

Table S6. Most common intersections of the replication sample's shallow PCC sulci. This table illustrates the different sulcal patterns, or types, of the three shallow PCC sulci identified in the replication young adult sample (N = 36 participants). For each sulcus, the top three most prevalent sulcal patterns and their percent of occurrence are provided for both the left (LH) and right hemispheres (RH). The incidence of each sulcus in this sample is also provided for each hemisphere for reference. The abbreviations used are as follows: callosal sulcus (*cas*); cingulate sulcus (*cgs*); inframarginal sulcus (*ifrms*); marginal ramus of the cingulate sulcus (*mcgs*); no intersections (*free*); posterior intracingulate sulcus (*icgs-p*); splenial sulcus (*spls*); subsplenial sulcus (*sspls*).

RAS coordinate	df	β	SE	t value	*p*-value	adjusted R^2	F-statistic	adjusted *p*-value
discovery								
right (LH)	1, 33	0.61	0.16	3.77	<0.001	0.28	14.23	<0.001
right (RH)	1, 34	0.50	0.17	2.87	0.007	0.17	8.23	0.007
anterior (LH)	1, 33	0.57	0.11	5.37	<0.001	0.45	28.84	<0.001
anterior (RH)	1, 34	0.44	0.10	4.46	<0.001	0.35	19.91	<0.001
superior (LH)	1, 33	0.98	0.10	9.68	<0.001	0.73	93.71	<0.001
superior (RH)	1, 34	0.74	0.08	9.65	<0.001	0.72	93.04	<0.001
replication								
right (LH)	1, 31	0.77	0.16	4.96	<0.001	0.42	24.61	<0.001
right (RH)	1, 32	1.14	0.39	2.91	0.007	0.18	8.44	0.007
anterior (LH)	1, 31	0.40	0.11	3.71	0.001	0.29	13.77	0.001
anterior (RH)	1,32	0.47	0.16	2.96	0.006	0.19	8.74	0.006
superior (LH)	1, 31	0.82	0.10	8.29	<0.001	0.68	68.80	<0.001
superior (RH)	1, 32	0.92	0.09	9.69	<0.001	0.74	93.95	<0.001

Table S7. Regression analysis summary for *ifrms* location predicting CCN-b location. This table provides the output of each linear regression run between each of the RAS (right, anterior, superior) coordinates of the inframarginal sulcus (*ifrms*; predictor variable) and cognitive control network B (CCN-b; outcome variable). A separate linear regression was run for each coordinate in each hemisphere (left (LH) and right (RH)) and sample (discovery and replication). The *p*-values presented in this table are FDR corrected for multiple comparisons. Exclusions: The LH of one participant in each sample was not included due to not having a CCN-b node near the *ifrms* and two participants from the replication sample were not included due to not having resting-state parcellations available. The other abbreviations used are as follows: degrees of freedom (df); regression beta coefficient (β); standard error (SE).

RAS coordinate	df	β	SE	t value	p-value	adjusted R^2	F-statistic	adjusted p-value
discovery								
right (LH)	1, 34	0.80	0.16	5.07	<0.001	0.41	25.75	<0.001
right (RH)	1, 34	0.32	0.09	3.43	0.002	0.23	11.74	0.002
anterior (LH)	1, 34	0.43	0.11	3.87	<0.001	0.28	14.94	<0.001
anterior (RH)	1, 34	0.30	0.09	3.38	0.002	0.23	11.43	0.002
superior (LH)	1, 34	0.90	0.10	8.69	<0.001	0.68	75.47	<0.001
superior (RH)	1, 34	0.71	0.08	9.31	<0.001	0.71	86.62	<0.001
replication								
right (LH)	1, 32	0.56	0.09	6.02	<0.001	0.52	36.21	<0.001
right (RH)	1, 32	0.55	0.14	3.82	<0.001	0.29	14.62	<0.001
anterior (LH)	1, 32	0.32	0.10	3.11	0.004	0.21	9.67	0.004
anterior (RH)	1,32	0.41	0.10	4.02	<0.001	0.32	16.19	<0.001
superior (LH)	1, 32	0.81	0.09	8.96	<0.001	0.71	80.29	<0.001
superior (RH)	1, 32	0.86	0.08	10.24	<0.001	0.76	104.90	<0.001

Table S8. Regression analysis summary for *ifrms* location predicting CCN-c location. This table provides the output of each linear regression run between each of the RAS (right, anterior, superior) coordinates of the inframarginal sulcus (*ifrms*; predictor variable) and cognitive control network C (CCN-c; outcome variable). A separate linear regression was run for each coordinate in each hemisphere (left (LH) and right (RH)) and sample (discovery and replication). The *p*-values presented in this table are FDR corrected for multiple comparisons. Exclusions: Two participants from the replication sample were not included due to not having resting-state parcellations available. The other abbreviations used are as follows: degrees of freedom (df); regression beta coefficient (β); standard error (SE).

sulci	appearance in LH	LH %	appearance in RH	RH %
pos	72/72	100.00	72/72	100.00
prculs	72/72	100.00	72/72	100.00
prcus-p	72/72	100.00	72/72	100.00
prcus-i	72/72	100.00	72/72	100.00
prcus-a	72/72	100.00	72/72	100.00
spls	72/72	100.00	72/72	100.00
sps	64/72	88.89	67/72	93.06
mcgs	72/72	100.00	72/72	100.00
sspls	38/72	52.78	34/72	47.22
ifrms	72/72	100.00	72/72	100.00
icgs-p	32/72	44.44	36/72	50.00

Table S9. Incidence rates of PMC sulci in the juvenile sample. This table illustrates the incidence rates of the 8-11 definable PMC sulci in the juvenile sample (N = 72 participants). The incidence rate of each sulcus (posterior to anterior) is provided in number and percent for both the left (LH) and right hemispheres (RH). The abbreviations used are as follows: anterior precuneal sulcus (*prcus-a*); intermediate precuneal sulcus (*prcus-i*); inframarginal sulcus (*ifrms*); marginal ramus of the cingulate sulcus (*mcgs*); parieto-occipital sulcus (*pos*); posterior intracingulate sulcus (*icgs-p*); posterior precuneal sulcus (*prcus-p*); precuneal limiting sulcus (*prculs*); splenial sulcus (*spls*); subsplenial sulcus (*sspls*); superior parietal sulcus (*sps*).

sulci	appearance in LH	LH %	appearance in RH	RH %
pos	72/72	100.00	72/72	100.00
prculs	72/72	100.00	72/72	100.00
prcus-p	72/72	100.00	72/72	100.00
prcus-i	72/72	100.00	72/72	100.00
prcus-a	72/72	100.00	72/72	100.00
spls	72/72	100.00	72/72	100.00
sps	59/72	81.94	55/72	76.39
mcgs	72/72	100.00	72/72	100.00
sspls	33/72	45.83	32/72	44.44
ifrms	72/72	100.00	72/72	100.00
icgs-p	27/72	37.50	28/72	38.89

Table S10. Incidence rates of PMC sulci in the healthy older adult sample. This table illustrates the incidence rates of the 8-11 definable PMC sulci in the healthy older adult sample (N = 72 participants). The incidence rate of each sulcus (posterior to anterior) is provided in number and percent for both the left (LH) and right hemispheres (RH). The abbreviations used are as follows: anterior precuneal sulcus (*prcus-a*); intermediate precuneal sulcus (*prcus-i*); inframarginal sulcus (*ifrms*); marginal ramus of the cingulate sulcus (*mcgs*); parieto-occipital sulcus (*pos*); posterior intracingulate sulcus (*icgs-p*); posterior precuneal sulcus (*prcus-p*); precuneal limiting sulcus (*prculs*); splenial sulcus (*spls*); subsplenial sulcus (*sspls*); superior parietal sulcus (*sps*).

Sulci	First	%	Second	%	Third	%
prcus-a						
LH (n=72)	*spls*	79.2	*prcus-i*	19.4	*mcgs*	9.7
RH (n=72)	*spls*	68.1	*prcus-i*	22.2	*free*	20.8
prcus-i						
LH (n=72)	*spls*	68.1	*prcus-a*	22.2	*free*	20.8
RH (n=72)	*spls*	61.1	*free*	31.9	*prcus-a*	22.2
prcus-p						
LH (n=72)	*spls*	55.6	*free*	33.3	*prcus-i*	15.3
RH (n=72)	*spls*	52.8	*free*	37.5	*prcus-i*	19.4

Table S11. Most common intersections of the juvenile sample's precuneal sulci. This table illustrates the different sulcal patterns, or types, of the three precuneal sulci (*prcus*) identified in the juvenile sample (N = 72 participants). For each sulcus, the top three most prevalent sulcal patterns and their percent of occurrence are provided for both the left (LH) and right hemispheres (RH). The incidence of each sulcus in this sample is also provided for each hemisphere for reference. The abbreviations used are as follows: anterior precuneal sulcus (*prcus-a*); intermediate precuneal sulcus (*prcus-i*); marginal ramus of the cingulate sulcus (*mcgs*); no intersections (*free*); posterior precuneal sulcus (*prcus-p*); splenial sulcus (*spls*).

Sulci	First	%	Second	%	Third	%
icgs-p						
LH (n=32)	*free*	75.0	*mcgs*	12.5	*cgs*	9.4
RH (n=36)	*free*	83.3	*cgs*	11.1	*ifrms*	2.8
ifrms						
LH (n=72)	*free*	80.6	*mcgs*	11.1	*spls*	8.3
RH (n=72)	*free*	73.6	*spls*	18.1	*mcgs*	5.6
sspls						
LH (n=38)	*free*	78.9	*cas*	15.8	*spls*	5.3
RH (n=34)	*free*	85.3	*cas*	11.8	*spls*	2.9

Table S12. Most common intersections of the juvenile sample's shallow PCC sulci. This table illustrates the different sulcal patterns, or types, of the three shallow PCC sulci identified in the juvenile sample (N = 72 participants). For each sulcus, the top three most prevalent sulcal patterns and their percent of occurrence are provided for both the left (LH) and right hemispheres (RH). The incidence of each sulcus in this sample is also provided for each hemisphere for reference. The abbreviations used are as follows: callosal sulcus (*cas*); cingulate sulcus (*cgs*); inframarginal sulcus (*ifrms*); marginal ramus of the cingulate sulcus (*mcgs*); no intersections (*free*); posterior intracingulate sulcus (*icgs-p*); splenial sulcus (*spls*); subsplenial sulcus (*sspls*).

Sulci	First	%	Second	%	Third	%
prcus-a						
LH (n=72)	*spls*	70.8	*free*	20.8	*prcus-i*	9.7
RH (n=72)	*spls*	75.0	*free*	15.3	*mcgs*	9.7
prcus-i						
LH (n=72)	*spls*	54.2	*free*	30.6	*prcus-a*	9.7
RH (n=72)	*spls*	52.8	*free*	38.9	*prcus-p*	13.9
prcus-p						
LH (n=72)	*free*	52.4	*spls*	44.4	*prcus-i*	6.9
RH (n=72)	*spls*	56.9	*free*	34.7	*prcus-i*	13.9

Table S13. Most common intersections of the healthy older adult sample's precuneal sulci. This table illustrates the different sulcal patterns, or types, of the three precuneal sulci (*prcus*) identified in the healthy older adult sample (N = 72 participants). For each sulcus, the top three most prevalent sulcal patterns and their percent of occurrence are provided for both the left (LH) and right hemispheres (RH). The incidence of each sulcus in this sample is also provided for each hemisphere for reference. The abbreviations used are as follows: anterior precuneal sulcus (*prcus-a*); intermediate precuneal sulcus (*prcus-i*); marginal ramus of the cingulate sulcus (*mcgs*); no intersections (*free*); posterior precuneal sulcus (*prcus-p*); splenial sulcus (*spls*).

Sulci	First	%	Second	%	Third	%
icgs-p						
LH (n=27)	*free*	88.9	*mcgs*	3.7	*cas*	3.7
RH (n=28)	*free*	82.1	*mcgs*	10.7	*cgs*	7.1
ifrms						
LH (n=72)	*free*	80.6	*mcgs*	9.7	*spls*	6.9
RH (n=72)	*free*	77.8	*spls*	13.9	*mcgs*	4.2
sspls						
LH (n=33)	*free*	69.7	*cas*	21.2	*spls*	9.1
RH (n=32)	*free*	87.5	*cas*	9.4	*spls*	3.1

Table S14. Most common intersections of the healthy older adult sample's shallow PCC sulci. This table illustrates the different sulcal patterns, or types, of the three shallow PCC sulci identified in the healthy older adult sample (N = 72 participants). For each sulcus, the top three most prevalent sulcal patterns and their percent of occurrence are provided for both the left (LH) and right hemispheres (RH). The incidence of each sulcus in this sample is also provided for each hemisphere for reference. The abbreviations used are as follows: callosal sulcus (*cas*); cingulate sulcus (*cgs*); inframarginal sulcus (*ifrms*); marginal ramus of the cingulate sulcus (*mcgs*); no intersections (*free*); posterior intracingulate sulcus (*icgs-p*); splenial sulcus (*spls*); subsplenial sulcus (*sspls*).

	mean	sd
pos		
j lh	20.00	2.51
ya lh	19.29	2.48
oa lh	19.87	2.30
j rh	20.36	2.51
ya rh	20.06	2.53
oa rh	20.34	2.09
prculs		
j lh	14.27	2.98
ya lh	13.97	2.92
oa lh	14.88	2.61
j rh	13.34	3.03
ya rh	13.82	3.17
oa rh	14.03	2.96
prcus-p		
j lh	8.67	3.51
ya lh	7.52	3.45
oa lh	6.92	3.06
j rh	7.50	3.49
ya rh	6.62	3.45
oa rh	6.00	3.11
prcus-i		
j lh	11.49	3.06
ya lh	9.42	3.30
oa lh	8.59	3.30
j rh	10.27	3.15
ya rh	9.43	3.26
oa rh	8.13	3.52
prcus-a		
j lh	11.76	2.47
ya lh	10.36	3.33
oa lh	10.26	2.71
j rh	10.19	2.97
ya rh	8.75	3.12
oa rh	8.30	2.79
sps		
j lh	13.42	2.78
ya lh	11.21	3.28
oa lh	10.71	3.19
j rh	11.94	3.53
ya rh	10.66	3.41
oa rh	10.84	3.36

spls		
j lh	13.48	1.74
ya lh	12.63	1.61
oa lh	12.35	1.91
j rh	12.37	1.77
ya rh	11.41	1.78
oa rh	10.73	1.88
mcgs		
j lh	16.26	1.62
ya lh	15.09	1.51
oa lh	15.26	1.58
j rh	14.70	1.87
ya rh	13.90	1.79
oa rh	14.22	1.39
sspls		
j lh	2.93	1.47
ya lh	2.60	1.32
oa lh	3.49	1.95
j rh	1.68	1.11
ya rh	1.55	0.91
oa rh	2.26	0.91
ifrms		
j lh	3.64	2.77
ya lh	2.59	0.98
oa lh	3.77	1.90
j rh	2.61	2.06
ya rh	2.14	1.85
oa rh	2.94	1.95
icgs-p		
j lh	3.59	2.33
ya lh	2.64	1.54
oa lh	3.07	1.31
j rh	1.67	1.10
ya rh	2.18	1.81
oa rh	2.61	1.61

Table S15. Mean ± std depth of each PMC sulcus between human age groups. Depth values are in millimeters. Abbreviations are as follows: juvenile (j), young adult (ya), older adult (oa), left hemisphere (lh), right hemisphere (rh).

	mean	sd
pos		
j lh	1006.85	270.56
ya lh	958.54	280.86
oa lh	947.81	247.88
j rh	1206.11	289.68
ya rh	1138.71	311.39
oa rh	1117.60	293.55
prculs		
j lh	351.92	169.98
ya lh	428.85	189.51
oa lh	394.94	177.06
j rh	343.65	192.04
ya rh	403.65	185.88
oa rh	386.03	189.75
prcus-p		
j lh	249.93	138.99
ya lh	209.86	155.11
oa lh	181.25	104.19
j rh	242.93	143.95
ya rh	204.99	125.99
oa rh	166.31	106.63
prcus-i		
j lh	328.17	156.50
ya lh	286.42	155.12
oa lh	236.79	131.24
j rh	332.92	163.39
ya rh	306.71	156.50
oa rh	278.53	158.74
prcus-a		
j lh	282.38	155.26
ya lh	274.86	206.74
oa lh	275.26	138.84
j rh	268.38	143.63
ya rh	231.62	137.72
oa rh	221.72	168.71
sps		
j lh	480.22	170.72
ya lh	442.32	212.44
oa lh	427.49	243.23
j rh	447.66	227.96
ya rh	410.97	183.18
oa rh	391.29	204.93

spls		
j lh	501.00	132.04
ya lh	510.28	146.03
oa lh	478.24	135.24
j rh	507.47	164.05
ya rh	491.22	143.83
oa rh	436.35	134.23
mcgs		
j lh	813.00	220.27
ya lh	804.42	175.57
oa lh	793.69	213.04
j rh	789.97	188.75
ya rh	734.32	201.28
oa rh	783.26	164.19
sspls		
j lh	45.08	32.46
ya lh	46.25	26.19
oa lh	44.61	36.25
j rh	43.50	29.98
ya rh	32.37	29.67
oa rh	43.56	23.76
ifrms		
j lh	79.97	42.92
ya lh	67.18	31.91
oa lh	61.60	46.50
j rh	82.36	49.34
ya rh	76.56	39.03
oa rh	56.96	30.13
icgs-p		
j lh	47.78	44.92
ya lh	34.44	20.52
oa lh	36.41	23.02
j rh	43.81	25.52
ya rh	37.09	20.09
oa rh	51.46	30.70

Table S16. Mean ± std surface area of each PMC sulcus between human age groups. Surface area values are in squared millimeters. Abbreviations are as follows: juvenile (j), young adult (ya), older adult (oa), left hemisphere (lh), right hemisphere (rh).

	mean	sd
pos		
j lh	2.56	0.20
ya lh	2.39	0.14
oa lh	2.15	0.20
j rh	2.63	0.16
ya rh	2.45	0.13
oa rh	2.20	0.18
prculs		
j lh	2.40	0.31
ya lh	2.24	0.20
oa lh	1.99	0.25
j rh	2.34	0.32
ya rh	2.27	0.21
oa rh	2.01	0.25
prcus-p		
j lh	2.78	0.44
ya lh	2.52	0.29
oa lh	2.32	0.29
j rh	2.71	0.44
ya rh	2.55	0.30
oa rh	2.34	0.34
prcus-i		
j lh	2.44	0.32
ya lh	2.40	0.27
oa lh	2.23	0.34
j rh	2.46	0.36
ya rh	2.40	0.25
oa rh	2.19	0.33
prcus-a		
j lh	2.53	0.32
ya lh	2.41	0.35
oa lh	2.09	0.28
j rh	2.54	0.38
ya rh	2.52	0.36
oa rh	2.16	0.33
sps		
j lh	2.13	0.21
ya lh	2.12	0.17
oa lh	1.96	0.23
j rh	2.16	0.28
ya rh	2.16	0.18
oa rh	1.97	0.25

spls		
j lh	2.91	0.21
ya lh	2.65	0.16
oa lh	2.46	0.20
j rh	2.92	0.24
ya rh	2.71	0.18
oa rh	2.45	0.18
mcgs		
j lh	2.42	0.17
ya lh	2.25	0.13
oa lh	2.05	0.21
j rh	2.36	0.17
ya rh	2.24	0.13
oa rh	2.02	0.17
sspls		
j lh	3.67	0.35
ya lh	3.17	0.33
oa lh	2.87	0.39
j rh	3.81	0.39
ya rh	3.18	0.36
oa rh	2.93	0.40
ifrms		
j lh	3.81	0.44
ya lh	3.43	0.36
oa lh	2.92	0.35
j rh	3.71	0.40
ya rh	3.44	0.34
oa rh	2.99	0.36
icgs-p		
j lh	3.57	0.52
ya lh	3.17	0.41
oa lh	2.78	0.46
j rh	3.66	0.33
ya rh	3.20	0.38
oa rh	2.84	0.44

Table S17. Mean ± std cortical thickness of each PMC sulcus between human age groups. Cortical thickness values are in millimeters. Abbreviations are as follows: juvenile (j), young adult (ya), older adult (oa), left hemisphere (lh), right hemisphere (rh).

participants	scanner manufacturer	magnetic field strength (T)	TR (ms)	TE (ms)	voxel size (mm^3)
26	Siemens	3	2300.0	3.0	1 x 1 x 1
8	Siemens	3	2300.0	3.0	1.1 x 1.1 x 1.2
6	Philips	3	6.5	2.9	1 x 1 x 1
6	GE	1.5	8.6	3.8	0.9 x 0.9 x 1.2
5	Philips	3	6.8	3.2	1 x 1 x 1.2
5	Siemens	3	2300.0	3.0	1 x 1 x 1.2
4	GE	1.5	8.9	3.9	0.9 x 0.9 x 1.2
2	Siemens	1.5	2400.0	3.5	1.3 x 1.3 x 1.2
2	GE	1.5	9.2	4.1	0.9 x 0.9 x 1.2
1	Philips	3	6.8	3.1	1 x 1 x 1.2
1	Philips	1.5	8.6	4.0	0.9 x 0.9 x 1.2
1	Philips	1.5	8.5	4.0	0.9 x 0.9 x 1.2
1	GE	1.5	9.2	4.0	0.9 x 0.9 x 1.2
1	GE	1.5	9.1	4.0	0.9 x 0.9 x 1.2
1	GE	1.5	7.0	3.9	0.9 x 0.9 x 1.2
1	GE	3	7.0	3.0	1 x 1 x 1.2
1	Siemens	1.5	3000.0	3.6	1.3 x 1.3 x 1.2

Table S18. Scanning parameters of the healthy older adult participants. This table illustrates the different scanning parameters used for each of our randomly selected, healthy older adult participants from the Alzheimer's Disease Neuroimaging Initiative (ADNI) online database (http://adni.loni.usc.edu). For each different set of parameters, the number of participants, scanner manufacturer, magnetic field strength in Teslas (T), repetition time (TR) in ms, time to echo (TE) in ms, and voxel size in mm^3 are provided.

REFERENCES AND NOTES

1. P. Rakic, Specification of cerebral cortical areas. *Science* **241**, 170–176 (1988).

2. W. Welker, in *Cerebral Cortex: Comparative Structure and Evolution of Cerebral Cortex, Part II*, E. G. Jones, A. Peters, Eds. (Springer US, 1990), pp. 3–136.

3. K. Zilles, N. Palomero-Gallagher, K. Amunts, Development of cortical folding during evolution and ontogeny. *Trends Neurosci.* **36**, 275–284 (2013).

4. D. C. Van Essen, C. J. Donahue, M. F. Glasser, Development and evolution of cerebral and cerebellar cortex. *Brain Behav. Evol.* **91**, 158–169 (2018).

5. K. Zilles, E. Armstrong, A. Schleicher, H.-J. Kretschmann, The human pattern of gyrification in the cerebral cortex. *Anat. Embryol.* **179**, 173–179 (1988).

6. D. C. Van Essen, in *Evolution of Nervous Systems*, J. H. Kaas, Ed. (Academic Press, 2007), pp. 267–276.

7. D. J. Cunningham, *Contribution to the Surface Anatomy of the Cerebral Hemispheres* (Academy House, 1892).

8. G. E. Smith, A new topographical survey of the human cerebral cortex, being an account of the distribution of the anatomically distinct cortical areas and their relationship to the cerebral sulci. *J. Anat. Physiol.* **41**, 237–254 (1907).

9. B. A. Wandell, J. Winawer, Imaging retinotopic maps in the human brain. *Vision Res.* **51**, 718–737 (2011).

10. N. C. Benson, O. H. Butt, R. Datta, P. D. Radoeva, D. H. Brainard, G. K. Aguirre, The retinotopic organization of striate cortex is well predicted by surface topology. *Curr. Biol.* **22**, 2081–2085 (2012).

11. K. S. Weiner, G. Golarai, J. Caspers, M. R. Chuapoco, H. Mohlberg, K. Zilles, K. Amunts, K. Grill-Spector, The mid-fusiform sulcus: A landmark identifying both cytoarchitectonic and functional

divisions of human ventral temporal cortex. *Neuroimage* **84**, 453–465 (2014).

12. K. S. Weiner, K. Zilles, The anatomical and functional specialization of the fusiform gyrus. *Neuropsychologia* **83**, 48–62 (2016).

13. K. S. Weiner, The mid-fusiform sulcus (*sulcus sagittalis gyri fusiformis*). *Anat. Rec.* **302**, 1491–1503 (2019).

14. G. C. Ribas, A. Yasuda, E. C. Ribas, K. Nishikuni, A. J. Rodrigues Jr., Surgical anatomy of microneurosurgical sulcal key points. *Oper. Neurosurg.* **59**, ONS177-210 (2006).

15. A. Fornito, M. Yücel, S. Wood, G. W. Stuart, J.-A. Buchanan, T. Proffitt, V. Anderson, D. Velakoulis, C. Pantelis, Individual differences in anterior cingulate/paracingulate morphology are related to executive functions in healthy males. *Cereb. Cortex* **14**, 424–431 (2004).

16. A. Fornito, M. Yücel, S. J. Wood, T. Proffitt, P. D. McGorry, D. Velakoulis, C. Pantelis, Morphology of the paracingulate sulcus and executive cognition in schizophrenia. *Schizophr. Res.***88**, 192–197 (2006).

17. G. Borst, A. Cachia, J. Vidal, G. Simon, C. Fischer, A. Pineau, N. Poirel, J.-F. Mangin, O. Houdé, Folding of the anterior cingulate cortex partially explains inhibitory control during childhood: A longitudinal study. *Dev. Cogn. Neurosci.* **9**, 126–135 (2014).

18. J. R. Garrison, C. Fernyhough, S. McCarthy-Jones, M. Haggard; Australian Schizophrenia Research Bank, J. S. Simons, Paracingulate sulcus morphology is associated with hallucinations in the human brain. *Nat. Commun.* **6**, 8956 (2015).

19. C. Amiez, C. R. E. Wilson, E. Procyk, Variations of cingulate sulcal organization and link with cognitive performance. *Sci. Rep.* **8**, 1–13 (2018).

20. A. Lopez-Persem, L. Verhagen, C. Amiez, M. Petrides, J. Sallet, The human ventromedial prefrontal cortex: Sulcal morphology and its influence on functional organization. *J. Neurosci.* **39**, 3627–3639 (2019).

21. J. A. Miller, W. I. Voorhies, D. J. Lurie, M. D'Esposito, K. S. Weiner, Overlooked tertiary sulci serve as a meso-scale link between microstructural and functional properties of human lateral prefrontal cortex. *J. Neurosci.* **41**, 2229–2244 (2021).

22. W. I. Voorhies, J. A. Miller, J. K. Yao, S. A. Bunge, K. S. Weiner, Cognitive insights from tertiary sulci in prefrontal cortex. *Nat. Commun.* **12**, 5122 (2021).

23. F. Sanides, Structure and function of the human frontal lobe. *Neuropsychologia* **2**, 209–219 (1964).

24. M. E. Raichle, A. M. MacLeod, A. Z. Snyder, W. J. Powers, D. A. Gusnard, G. L. Shulman, A default mode of brain function. *Proc. Natl. Acad. Sci. U.S.A.* **98**, 676–682 (2001).

25. R. L. Buckner, J. R. Andrews-Hanna, D. L. Schacter, The brain's default network: Anatomy, function, and relevance to disease. *Ann. N. Y. Acad. Sci.* **1124**, 1–38 (2008).

26. R. Leech, J. Smallwood, The posterior cingulate cortex: Insights from structure and function. *Cingulate Cortex*, **166**, 73–85 (2019).

27. J. Smallwood, B. C. Bernhardt, R. Leech, D. Bzdok, E. Jefferies, D. S. Margulies, The default mode network in cognition: A topographical perspective. *Nat. Rev. Neurosci.* **22**, 503–513 (2021).

28. D. L. Schacter, D. R. Addis, R. L. Buckner, Remembering the past to imagine the future: The prospective brain. *Nat. Rev. Neurosci.* **8**, 657–661 (2007).

29. P. Hagmann, L. Cammoun, X. Gigandet, R. Meuli, C. J. Honey, V. J. Wedeen, O. Sporns, Mapping the structural core of human cerebral cortex. *PLOS Biol.* **6**, e159 (2008).

30. D. S. Margulies, J. L. Vincent, C. Kelly, G. Lohmann, L. Q. Uddin, B. B. Biswal, A. Villringer, F. Xavier Castellanos, M. P. Milham, M. Petrides, Precuneus shares intrinsic functional architecture in humans and monkeys. *Proc. Natl. Acad. Sci. U.S.A.* **106**, 20069–20074 (2009).

31. J. M. Pearson, S. R. Heilbronner, D. L. Barack, B. Y. Hayden, M. L. Platt, Posterior cingulate cortex: Adapting behavior to a changing world. *Trends Cogn. Sci.* **15**, 143–151 (2011).

32. R. Leech, D. J. Sharp, The role of the posterior cingulate cortex in cognition and disease. *Brain* **137**,

12–32 (2014).

33. H. Grydeland, L. T. Westlye, K. B. Walhovd, A. M. Fjell, Intracortical posterior cingulate myelin content relates to error processing: Results from T1- and T2-weighted MRI myelin mapping and electrophysiology in healthy adults. *Cereb. Cortex* **26**, 2402–2410 (2016).

34. J. Parvizi, G. W. Van Hoesen, J. Buckwalter, A. Damasio, Neural connections of the posteromedial cortex in the macaque. *Proc. Natl. Acad. Sci. U.S.A.* **103**, 1563–1568 (2006).

35. D. S. Margulies, S. S. Ghosh, A. Goulas, M. Falkiewicz, J. M. Huntenburg, G. Langs, G. Bezgin, S. B. Eickhoff, F. X. Castellanos, M. Petrides, E. Jefferies, J. Smallwood, Situating the default-mode network along a principal gradient of macroscale cortical organization. *Proc. Natl. Acad. Sci. U.S.A.* **113**, 12574–12579 (2016).

36. T. Xu, K.-H. Nenning, E. Schwartz, S.-J. Hong, J. T. Vogelstein, A. Goulas, D. A. Fair, C. E. Schroeder, D. S. Margulies, J. Smallwood, M. P. Milham, G. Langs, Cross-species functional alignment reveals evolutionary hierarchy within the connectome. *Neuroimage* **223**, 117346 (2020).

37. V. J. Sydnor, B. Larsen, D. S. Bassett, A. Alexander-Bloch, D. A. Fair, C. Liston, A. P. Mackey, M. P. Milham, A. Pines, D. R. Roalf, J. Seidlitz, T. Xu, A. Raznahan, T. D. Satterthwaite, Neurodevelopment of the association cortices: Patterns, mechanisms, and implications for psychopathology. *Neuron* **109**, 2820–2846 (2021).

38. R. L. Buckner, L. M. DiNicola, The brain's default network: Updated anatomy, physiology and evolving insights. *Nat. Rev. Neurosci.* **20**, 593–608 (2019).

39. J. A. Miller, M. D'Esposito, K. S. Weiner, Using tertiary sulci to map the "cognitive globe" of prefrontal cortex. *J. Cogn. Neurosci.*, 1–18 (2021).

40. M. Petrides, *Atlas of the Morphology of the Human Cerebral Cortex on the Average MNI Brain* (Academic Press, 2019).

41. R. Kong, J. Li, C. Orban, M. R. Sabuncu, H. Liu, A. Schaefer, N. Sun, X.-N. Zuo, A. J. Holmes, S. B. Eickhoff, B. T. T. Yeo, Spatial topography of individual-specific cortical networks predicts

human cognition, personality, and emotion. *Cereb. Cortex* **29**, 2533–2551 (2019).

42. E. M. Gordon, T. O. Laumann, A. W. Gilmore, D. J. Newbold, D. J. Greene, J. J. Berg, M. Ortega, C. Hoyt-Drazen, C. Gratton, H. Sun, J. M. Hampton, R. S. Coalson, A. L. Nguyen, K. B. McDermott, J. S. Shimony, A. Z. Snyder, B. L. Schlaggar, S. E. Petersen, S. M. Nelson, N. U. F. Dosenbach, Precision functional mapping of individual human brains. *Neuron* **95**, 791–807.e7 (2017).

43. M. F. Glasser, T. S. Coalson, E. C. Robinson, C. D. Hacker, J. Harwell, E. Yacoub, K. Ugurbil, J. Andersson, C. F. Beckmann, M. Jenkinson, S. M. Smith, D. C. Van Essen, A multi-modal parcellation of human cerebral cortex. *Nature***536**, 171–178 (2016).

44. T. Yarkoni, R. A. Poldrack, T. E. Nichols, D. C. Van Essen, T. D. Wager, Large-scale automated synthesis of human functional neuroimaging data. *Nat. Methods* **8**, 665–670 (2011).

45. L. Q. Uddin, R. F. Betzel, J. R. Cohen, J. S. Damoiseaux, F. De Brigard, S. Eickhoff, A. Fornito, C. Gratton, E. M. Gordon, A. Laird, L. J. Larson-Prior, A. R. McIntosh, L. D. Nickerson, L. P. Ana L. Pinho, R. Poldrack, A. Razi, S. Sadaghiani, J. M. Shine, A. Yendiki, B. T. Thomas Yeo, R. N. Spreng, Controversies and current progress on large-scale brain network nomenclature from OHBM WHATNET: Workgroup for HArmonized Taxonomy of NETworks (2022).

46. M. Ono, S. Kubik, C. D. Abernathey, *Atlas of the Cerebral Sulci* (G. Thieme Verlag, 1990).

47. L. Borne, D. Rivière, M. Mancip, J.-F. Mangin, Automatic labeling of cortical sulci using patch- or CNN-based segmentation techniques combined with bottom-up geometric constraints. *Med. Image Anal.* **62**, 101651 (2020).

48. K. Drudik, V. Zlatkina, M. Petrides, Morphological patterns and spatial probability maps of the superior parietal sulcus in the human brain. *Cereb. Cortex*, bhac132 (2022).

49. G. Retzius, *Das Menschenhirn: Studien in der makroskopischen Morphologie* (Königliche Buchdruckerei P. A. Norstedt & Söner, 1896).

50. J. Gomez, Z. Zhen, K. S. Weiner, Human visual cortex is organized along two genetically opposed

hierarchical gradients with unique developmental and evolutionary origins. *PLOS Biol.* **17**, e3000362 (2019).

51. X. Chen, X. Liu, B. J. Parker, Z. Zhen, K. S. Weiner, Functionally and structurally distinct fusiform face area(s) in over 1000 participants. bioRxiv 2022.04.08.487562 (2022).

52. V. S. Natu, J. Gomez, M. Barnett, B. Jeska, E. Kirilina, C. Jaeger, Z. Zhen, S. Cox, K. S. Weiner, N. Weiskopf, K. Grill-Spector, Apparent thinning of human visual cortex during childhood is associated with myelination. *Proc. Natl. Acad. Sci. U.S.A.* **116**, 20750–20759 (2019).

53. J. A. Miller, W. I. Voorhies, X. Li, I. Raghuram, N. Palomero-Gallagher, K. Zilles, C. C. Sherwood, W. D. Hopkins, K. S. Weiner, Sulcal morphology of ventral temporal cortex is shared between humans and other hominoids. *Sci. Rep.* **10**, 17132 (2020).

54. C. Amiez, J. Sallet, W. D. Hopkins, A. Meguerditchian, F. Hadj-Bouziane, S. Ben Hamed, C. R. E. Wilson, E. Procyk, M. Petrides, Sulcal organization in the medial frontal cortex provides insights into primate brain evolution. *Nat. Commun.* **10**, 3437 (2019).

55. M. Yucel, G. W. Stuart, P. Maruff, D. Velakoulis, S. F. Crowe, G. Savage, C. Pantelis, Hemispheric and gender-related differences in the gross morphology of the anterior cingulate/paracingulate cortex in normal volunteers: An MRI morphometric study. *Cerebral. Cortex* **11**, 17–25 (2001).

56. I. Lyu, S. Bao, L. Hao, J. Yao, J. A. Miller, W. Voorhies, W. D. Taylor, S. A. Bunge, K. S. Weiner, B. A. Landman, Labeling lateral prefrontal sulci using spherical data augmentation and context-aware training. *Neuroimage* **229**, 117758 (2021).

57. B. A. Vogt, L. Vogt, S. Laureys, Cytology and functionally correlated circuits of human posterior cingulate areas. *Neuroimage* **29**, 452–466 (2006).

58. B. A. Vogt, N. Palomero-Gallagher, in *The Human Nervous System (Third Edition)*, J. K. Mai, G. Paxinos, Eds. (Academic Press, 2012), pp. 943–987.

59. K. Amunts, H. Mohlberg, S. Bludau, K. Zilles, Julich-Brain: A 3D probabilistic atlas of the human brain's cytoarchitecture. *Science* **369**, 988–992 (2020).

60. E. M. Gordon, C. J. Lynch, C. Gratton, T. O. Laumann, A. W. Gilmore, D. J. Greene, M. Ortega, A. L. Nguyen, B. L. Schlaggar, S. E. Petersen, N. U. F. Dosenbach, S. M. Nelson, Three distinct sets of connector hubs integrate human brain function. *Cell Rep.* **24**, 1687–1695.e4 (2018).

61. B. Y. Hayden, A. C. Nair, A. N. McCoy, M. L. Platt, Posterior cingulate cortex mediates outcome-contingent allocation of behavior. *Neuron* **60**, 19–25 (2008).

62. B. Y. Hayden, D. V. Smith, M. L. Platt, Electrophysiological correlates of default-mode processing in macaque posterior cingulate cortex. *Proc. Natl. Acad. Sci U.S.A.* **106**, 5948–5953 (2009).

63. B. A. Vogt, L. Vogt, N. B. Farber, G. Bush, Architecture and neurocytology of monkey cingulate gyrus. *J. Comp. Neurol.***485**, 218–239 (2005).

64. E. Armstrong, A. Schleicher, H. Omran, M. Curtis, K. Zilles, The ontogeny of human gyrification. *Cereb. Cortex.* **5**, 56–63 (1995).

65. J. G. Chi, E. C. Dooling, F. H. Gilles, Gyral development of the human brain. *Ann. Neurol.* **1**, 86–93 (1977).

66. L. Brun, G. Auzias, M. Viellard, N. Villeneuve, N. Girard, F. Poinso, D. Da Fonseca, C. Deruelle, Localized misfolding within Broca's area as a distinctive feature of autistic disorder. *Biol. Psychiatry Cogn. Neurosci. Neuroimaging* **1**, 160–168 (2016).

67. C. J. Ammons, M.-E. Winslett, J. Bice, P. Patel, K. E. May, R. K. Kana, The mid-fusiform sulcus in autism spectrum disorder: Establishing a novel anatomical landmark related to face processing. *Autism Res.* **14**, 53–64 (2021).

68. C. J. Lynch, L. Q. Uddin, K. Supekar, A. Khouzam, J. Phillips, V. Menon, Default mode network in childhood autism: Posteromedial cortex heterogeneity and relationship with social deficits. *Biol. Psychiatry* **74**, 212–219 (2013).

69. D. C. Van Essen, K. Ugurbil, E. Auerbach, D. Barch, T. E. J. Behrens, R. Bucholz, A. Chang, L. Chen, M. Corbetta, S. W. Curtiss, S. D. Penna, D. Feinberg, M. F. Glasser, N. Harel, A. C. Heath, L. Larson-Prior, D. Marcus, G. Michalareas, S. Moeller, R. Oostenveld, S. E. Petersen, F. Prior, B. L.

Schlaggar, S. M. Smith, A. Z. Snyder, J. Xu, E. Yacoub; WU-Minn HCP Consortium, The human connectome project: A data acquisition perspective. *Neuroimage* **62**, 2222–2231 2012).

70. A. M. Dale, B. Fischl, M. I. Sereno, Cortical surface-based analysis. I. Segmentation and surface reconstruction. *Neuroimage* **9**, 179–194 (1999).

71. B. Fischl, M. I. Sereno, A. M. Dale, Cortical surface-based analysis. II: Inflation, flattening, and a surface-based coordinate system. *Neuroimage* **9**, 195–207 (1999).

72. B. Fischl, M. I. Sereno, R. B. Tootell, A. M. Dale, High-resolution intersubject averaging and a coordinate system for the cortical surface. *Hum. Brain Mapp.* **8**, 272–284 (1999).

73. M. F. Glasser, S. N. Sotiropoulos, J. A. Wilson, T. S. Coalson, B. Fischl, J. L. Andersson, J. Xu, S. Jbabdi, M. Webster, J. R. Polimeni, D. C. Van Essen, M. Jenkinson; WU-Minn HCP Consortium, The minimal preprocessing pipelines for the human connectome project. *Neuroimage* **80**, 105–124 (2013).

74. B. A. Vogt, E. A. Nimchinsky, L. J. Vogt, P. R. Hof, Human cingulate cortex: Surface features, flat maps, and cytoarchitecture. *J. Comp. Neurol.***359**, 490–506 (1995).

75. C. R. Madan, Robust estimation of sulcal morphology. *Brain Inform.* **6**, 5 (2019).

76. B. Fischl, A. M. Dale, Measuring the thickness of the human cerebral cortex from magnetic resonance images. *Proc. Natl. Acad. Sci. U.S.A.* **97**, 11050–11055 (2000).

77. M. F. Glasser, D. C. Van Essen, Mapping human cortical areas in vivo based on myelin content as revealed by T1- and T2-weighted MRI. *J. Neurosci.* **31**, 11597–11616 (2011).

78. E. Ferrer, K. J. Whitaker, J. S. Steele, C. T. Green, C. Wendelken, S. A. Bunge, White matter maturation supports the development of reasoning ability through its influence on processing speed. *Dev. Sci.* **16**, 941–951 (2013).

79. S. S. Keller, N. Roberts, W. Hopkins, A comparative magnetic resonance imaging study of the anatomy, variability, and asymmetry of Broca's area in the human and chimpanzee brain. *J.*

Neurosci. **29**, 14607–14616 (2009).

80. W. D. Hopkins, X. Li, T. Crow, N. Roberts, Vertex- and atlas-based comparisons in measures of cortical thickness, gyrification and white matter volume between humans and chimpanzees. *Brain Struct. Funct.***222**, 229–245 (2017).

81. R. Gustaf, *Cerebra simiarum illustrata. Das Affenhirn in bildlicher Darstellung* (Stockholm,Centraldruckerei, 1906).

82. E. M. Gordon, T. O. Laumann, B. Adeyemo, A. W. Gilmore, S. M. Nelson, N. U. F. Dosenbach, S. E. Petersen, Individual-specific features of brain systems identified with resting state functional correlations. *Neuroimage* **146**, 918–939 (2017).

83. A. Ecker. *Die Hirnwindungen des Menschen* (F. Vieweg u. Sohn, 1869).

84. E. Huschke, *Schaedel, Hirn und Seele des Menschen und der Thiere nach Alter, Geschlecht und Race: dargestellt nach neuen Methoden und Untersuchungen* (Mauke, 1854).

85. A. Ecker, *On the Convolutions of the Human Brain* (Smith, Elder & Company, 1873).

86. H. J. ten Donkelaar, D. Kachlík, R. Shane Tubbs, *An Illustrated Terminologia Neuroanatomica: A Concise Encyclopedia of Human Neuroanatomy* (Springer, 2018).

87. H. J. T. ten Donkelaar, H. J. ten Donkelaar, N. Tzourio-Mazoyer, J. K. Mai, Toward a common terminology for the gyri and sulci of the human cerebral cortex. *Front. Neuroanat.* **12**, 93 (2018).

88. E. A. Spitzka, The post-mortem examination of Leon F. Czolgosz, the assassin of President McKinley. *Am. J. Psychiatry* **58**, 386–404 (1902).

89. E. A. Spitzka, A study of the brains of six eminent scientists and scholars belonging to the American Anthropometric Society, together with a description of the skull of Professor E. D. Cope. *Trans. Am. Philos. Soc.* **21**, 175 (1907).

90. S. F. Witelson, D. L. Kigar, T. Harvey, The exceptional brain of Albert Einstein. *Lancet* **353**, 2149–2153 (1999).

91. D. Falk, F. E. Lepore, A. Noe, The cerebral cortex of Albert Einstein: A description and preliminary analysis of unpublished photographs. *Brain* **136**, 1304–1327 (2013).

92. K. S. Weiner, On (ab)normality: Einstein's fusiform gyrus. *Brain Cogn.* **94**, 1–3 (2015).

93. W. Men, D. Falk, T. Sun, W. Chen, J. Li, D. Yin, L. Zang, M. Fan, The corpus callosum of Albert Einstein's brain: Another clue to his high intelligence? *Brain* **137**, e268 (2014).

94. D. Falk, New information about Albert Einstein's brain. *Front. Evol. Neurosci.* **1**, 3 (2009).

95. D. Falk, Evolution of brain and culture: The neurological and cognitive journey from Australopithecus to Albert Einstein. *J. Anthropol. Sci.* **94**, 99–111 (2016).

96. A. M. Galaburda, Albert Einstein's brain. *Lancet* **354**, 1821–1822 (1999).

97. T. Hines, Neuromythology of Einstein's brain. *Brain Cogn.* **88**, 21–25 (2014).

98. A. W. Campbell, E. B. Schlesinger, H. A. Riley, *Histological Studies on the Localisation of Cerebral Function* (Cambridge Univ. Press, 1905).

99. H. Gray, *Anatomy of the Human Body* (Lea & Febiger, 1878).

100. C. Vogt, O. Vogt, *Allgemeine Ergebnisse unserer Hirnforschung* (J. A. Barth, 1919).

101. C. F. von Economo, G. N. Koskinas, *Die cytoarchitektonik der hirnrinde deserwachsenen menschen* (J. Springer, 1925).

102. P. Bailey, G. von Bonin, *The Isocortex of Man* (University of Illinois Press, 1951).

103. B. A. Vogt, Structural organization of cingulate cortex: Areas, neurons, and somatodendritic transmitter receptors, in *Neurobiology of Cingulate Cortex and Limbic Thalamus*, B. A. Vogt, M. Gabriel, Eds. (Birkhauser, 1993), pp. 19–70.

104. B. A. Vogt, Ed., *Cingulate Neurobiology and Disease* (OUP, 2009).